An unstructured finite-volume Level Set / Front Tracking method for two-phase flows with large density-ratios

Jun Liu, Tobias Tolle, Dieter Bothe, Tomislav Marić*

Mathematical Modeling and Analysis, Technische Universität Darmstadt

Abstract

This is the preprint version of the published manuscript `https://doi.org/10.1016/j.jcp.2023.112426`**: please cite the published manuscript when refering to the contents of this document.**

We extend the unstructured **LE**vel set / fro**NT** tracking (LENT) method [1, 2] for handling two-phase flows with strongly different densities (high-density ratios) by providing the theoretical basis for the numerical consistency between the mass and momentum conservation in the collocated Finite Volume discretization of the single-field two-phase Navier-Stokes equations. Our analysis provides the theoretical basis for the mass conservation equation introduced by Ghods and Herrmann [3] and used in [4, 5, 6, 7, 8]. We use a mass flux that is consistent with mass conservation in the implicit Finite Volume discretization of the two-phase momentum convection term, and solve the single-field Navier-Stokes equations with our SAAMPLE segregated solution algorithm [2]. The proposed ρLENT method recovers exact numerical stability for the two-phase momentum advection of a spherical droplet with density ratios $\rho^-/\rho^+ \in [1, 10^4]$. Numerical stability is demonstrated for in terms of the relative L_∞ velocity error norm, for density-ratios in the range of $[1, 10^4]$, dynamic viscosity-ratios in the range of $[1, 10^4]$ and very strong surface tension forces, for challenging mercury/air and water/air fluid pairings. In addition, the solver performs well in cases characterized by strong interaction between two phases, i.e., oscillating droplets and rising bubbles. The proposed ρLENT method[1] is applicable to any other two-phase flow simulation method that discretizes the single-field two-phase Navier-Stokes Equations using the collocated unstructured Finite Volume Method but does not solve an advection equation for the phase indicator using a flux-based approach, by adding the proposed geometrical approximation of the mass flux and the auxiliary mass conservation equation to the solution algorithm.

Keywords:
level set, front tracking, finite volume, unstructured mesh, high density ratios

*Corresponding author
Email addresses: `jun.liu@tu-darmstadt.de` (Jun Liu), `tolle@mma.tu-darmstadt.de` (Tobias Tolle), `bothe@mma.tu-darmstadt.de` (Dieter Bothe), `maric@mma.tu-darmstadt.de` (Tomislav Marić)

[1]The implementation in OpenFOAM is publicly available at `https://gitlab.com/leia-methods/lent/-/tree/2022-02-rhoLENT-R1` [9].

1. Introduction

A variety of natural and industrial two-phase flow processes involve gas/liquid flows, characterized by density ratios $\rho^-/\rho^+ \geq 10^3$[2], such as the atomization of fuel jets [10], sloshing tank [11], mold filing [12], water flooding [13]. Large density ratios at the fluid interface cause severe challenges for numerical simulations [14]. For segregated solvers, the discrete pressure Poisson equation becomes ill-conditioned if density is cell-centered, since its abrupt change across the interface between the two fluids can lead to a large variation in the matrix coefficients. Additionally, spurious numerical errors in the solution of the momentum equation accumulate because of inconsistencies between mass and momentum advection. Ghods and Herrmann [3] point out that for level set methods mass and momentum are typically transported in different, inconsistent ways. While mass is transported by a solution of the level set equation, momentum is obtained from solving a non-conservative form of a momentum balance equation. Hence, a large non-physical change in the momentum can be generated by a small error in the interface position when the density ratio is high. Nangia et al. [4] state that the abrupt change in density often introduces notable shear at the interface and adds difficulties in the discretization of governing momentum equations at the interface, which further leads to higher stiffness of the linear equation system.

Many researchers have addressed these problems, and some indicated further that because of the sizeable numerical error resulting from high-density ratios, some flow algorithms or solvers can only be used to solve low density-ratio cases with $\rho^-/\rho^+ \in [1, 10]$ [5]. However, in engineering applications, density ratios usually range from 10^2 to 10^3, and even 10^4 for molten metals or water-water vapor systems. Hence, a solution algorithm with the ability to handle a broader range of density ratio problems is required to simulate real-world engineering problems.

A pioneering attempt to alleviate numerical instability of the VOF method caused by high-density ratios was made by Rudman [15]. Rudman [15] has used a sub-mesh with a doubled mesh resolution for advecting volume fractions, compared to the mesh used for the momentum and pressure equations. The goal of this two mesh approach was the reduction of small errors in the discrete momentum that cause large errors in the velocity. However, an additional higher mesh resolution for the volume fractions requires a discrete divergence free velocity on the finer mesh. Furthermore, using an additional mesh for the volume fractions increases the computational costs significantly, and it is not applicable to general unstructured meshes. Rudman [15] demonstrates qualitatively a reduction of parasitic currents for the stationary droplet case with $\rho^-/\rho^+ = 100$, and improved results for more complex cases. Another important finding of Rudman [15] is the role of the densities used in the mass flux and the momentum flux in ensuring numerical consistency of the two-phase momentum advection.

Bussmann et al. [16] extended the work of Rudman [15] for the unstructured collocated finite volume method. Bussmann et al. [16] employ the conservative form for the momentum convection. At first, the momentum advection is solved separately, using an explicit Euler time integration scheme. Bussmann et al. [16] use the unstructured unsplit Volume-of-Fluid method of Rider and Kothe [17], which enables the simplification of the numerical consistency requirement for the density and momentum equations. Specifically, the solution of the volume fraction equation results in phase-specific volumes at face centers. Those phase-specific volumes are then used to compute the volume fractions at face centers. These volume fractions are used by Bussmann et al. [16], together with a simple average of cell densities, and velocities calculated by the least squares reconstruction

[2] In this publication ρ^- denotes the density of the denser fluid, so that $\rho^- \geq \rho^+$ and $\rho^-/\rho^+ \geq 1$ holds.

technique, to compute the momentum fluxes at face centers. Since the velocity is continuous at the interface, the least squares approximation is acceptable. However, calculating face-centered densities by an average does not yield numerical stability in all cases. Contrary to Rudman [15], Bussmann et al. [16] do not require an additional finer mesh. They do, however, limit the solution to first-order accuracy in time and introduce the CFL condition by solving the momentum advection equation explicitly. Bussmann et al. [16] introduce the important case of a translating droplet in a quiescent ambient fluid. This test case can be used to demonstrate numerical consistency in the momentum transport. Their solutions show accurate results for high density ratios, especially considering the fact that even the unsplit VOF method distorts the interface during the translation [18]. However, for $\rho^-/\rho^+ \in [1, 10^2]$, the constant translation velocity is modified by the solution of the pressure and momentum equations, which implies a remaining numerical inconsistency in this approach.

Sussman et al. [19] employ the CLSVOF method [20] for obtaining a robust and stable solution for the density ratio of 1000 by extrapolating the liquid velocities into the gas domain. The interface is advected using the extrapolated liquid velocity field only.

Raessi and Pitsch [5] propose a 2D staggered discretization of conservative single-field form of two-phase Navier-Stokes equations for handling high density ratios. Like Bussmann et al. [16] did, Raessi and Pitsch [5] first solve the momentum advection equation, using second-order (or higher) explicit integration schemes, and upwinding for the velocity near the interface. The density used in the momentum convective term is computed as a weighted combination of signed distances from the old and the new time step. For the partially submerged line segments bounding 2D rectangular cells, intersection between the mesh and the zero level set (iso-surface) is performed using the marching cubes algorithm. Raessi and Pitsch [5] point out that there is still an inconsistency between the face-centered density and the momentum transport, as the Level Set equation remains decoupled / inconsistent with the momentum transport. The verification of numerical stability was done using the translating droplet case from Bussmann et al. [16], and results demonstrate qualitative improvement for the density ratio $\rho^-/\rho^+ = 10^6$. Other density ratios have not been verified. A viscous oscillating droplet case demonstrates quantitative improvement in terms of the improved amplitude decay rate, compared to non-conservative form of the momentum equation.

Le Chenadec and Pitsch [21] extend their forward/backward Lagrangian tracking and Eulerian remapping VOF method [21] for handling high density ratios. Equivalent to volume fractions in [21], the density and the momentum are advected in the Lagrangian forward/backward tracking step by observing the control volume as a material volume and moving the mesh forward / backward with the flow velocity. While the content of material volumes does not change on the continuum level, this condition cannot be discretely ensured and is a source of conservation errors. In the Eulerian re-mapping step, physical properties are transferred from the Lagrangian to the Eulerian mesh, and the geometrical intersections between the PLIC interface on the forward/backward image of the mesh, and the background mesh, are another source of volume conservation errors. Ensuring numerical consistency further requires the transfer of velocities located at the center of mass. Since the velocities associated with the cell centroids are used, an inconsistency is introduced. Qualitative results show significant improvements for the stationary droplet with $\rho^-/\rho^+ = 10^9$, and quantitative improvement is shown for the standing wave by Prosperetti [22] with $\rho^-/\rho^+ = 850$.

Ghods and Herrmann [3] have developed a Consistent Rescaled momentum transport (CRMT) method. The CRMT method discretizes the conservative form of the single-field Navier-Stokes equations using a collocated unstructured Finite Volume method. To increase the numerical stability for high density ratio, CRMT solves what we call an "auxiliary" mass conservation equation using a mass flux either by upwinding the face-centered density in the interface cells and their face-

neighbors (defined by a volume fraction tolerance), or by averaging the densities elsewhere. The same discretization scheme used for the face-centered density is also applied to the mass flux in the convective term of the momentum equation. A difference is therefore introduced in the mass flux of the continuity equation and the mass flux in the convective term of the momentum equation when upwinding is used, because the upwinded face-centered density in the continuity equation uses the face-centered velocity, while the upwinded mass flux in the momentum equation includes both the upwind velocity and density. We show that any difference in the discretization of the mass flux to be a source of numerical inconsistency for the two-phase momentum advection. Like Bussmann et al. [16], the explicit discretization of the momentum convective term introduces the CFL condition, limiting the time step for convection-dominated multiphase flows, where high density ratios play a major role. Using upwind schemes makes the discretization first-order accurate. The droplet translation case [16], with $\rho^-/\rho^+ = 10^6$, is compared in terms of the droplet shape, that remains stable. Other density ratios are not reported for this verification case. It is our opinion, that the droplet shape errors may result from the interface advection scheme[3], and should be generally substituted by the L_∞ norm of the velocity error to demonstrate numerical consistency.

Vaudor et al. [23] base their approach on a CLSVOF code from Ménard et al. [24] and Aniszewski et al. [25], which can switch between LS-based and VOF-based mode to calculate momentum fluxes. They [23] chose the VOF-based momentum fluxes calculation mode and implemented the framework of Rudman's method [15] but with more accurate interpolation schemes for velocities and velocity gradients on faces of staggered meshes to ensure consistency. This method is developed in two-dimensions and exploits two sets of meshes. To provide a more widely applicable method, Vaudor et al. [26] advanced the method in their more recent study. In contrast to the previous work [23], the LS method tracks the interface, while the VOF method is utilized to update density. They exploited the identical scheme to discretize conservative convective term in mass and momentum equation. In addition, the mass flux is also identical in both discretized equations. A new strategy that leverages half cell-faces' and half cells' quantities of volume fraction and density to couple staggered mass cells and momentum cells is introduced to avoid the need for a refined mesh in the original method by Rudman [15]. A prominent feature of this new method is that it can be used to simulate three-dimensional applications. Besides, comparing with the method from Rudman [15], the new method shows relatively low computational cost when simulating the same 2D application.

Owkes and Desjardins [27] presented a three-dimensional, unsplit, second-order semi-Lagrangian VOF scheme that conserves mass and momentum and ensures consistency between the mass (volume fraction) and momentum fluxes. The volume fractions are geometrically transported near the fluid interface using the method from [28]. As in [15], Owkes and Desjardins [27] introduce an additional refined mesh for the calculation of semi-Lagrangian fluxes. The motivation for the refined mesh is to enforce the consistency between semi-Lagrangian mass and momentum fluxes, similar to Rudman [15]. Results confirm mass and momentum conservation, and stability of the momentum convection. The method proposed by Owkes and Desjardins [27] relies on the staggered variable arrangement and this, together with the use of the additional finer mesh, makes this approach inapplicable to unstructured finite volume meshes.

Orazzo et al. [6], similarly to Rudman [15], resolve the volume fraction function on twice finer sub-cells and update density from the volume fraction. After that, they update face-centered density on mass cells by averaging density on sub-cells, and then evaluate the mass flux on the faces of

[3]The Level Set and VoF methods do not exactly preserve the shape of a translating droplet.

standard staggered momentum cells. These density and mass flux values are used to initialize and calculate interim momentum and velocity during the prediction step. Zuzio et al. [7] made no changes and applied Orazzo's method [6]. Besides, they further verified and validated this method with more complex cases, e.g., liquid jet in cross-flow. Yang et al. [29] notice that the high-density ratio has a profound effect on robustly simulating two-phase flows at high Reynolds numbers. To mitigate the problem, they adopt the consistent framework from Nangia et al. [4] and replace the interface-capturing method in [4], which is standard LS, with CLSVOF method [20] to ensure mass conservation.

Patel and Natarajan [30] employ the method of Ghods and Herrmann [3], a high-resolution scheme called Cubic Upwind Interpolation (CUI) for the convective terms of momentum and volume fraction transport equations, and the solution of a momentum equation in the face-normal direction. The face-normal momentum equation leads to a combined collocated/staggered variable arrangement, that requires the use of nonlinear solvers, as this equation is a non-linear algebraic equation. Patel and Natarajan [30] demonstrate the balanced nature of their discretization for the stationary droplet using exact curvature and density ratios $\rho^-/\rho^+ \in [10, 1000]$. Numerical stability is demonstrated with reduced parasitic currents when the curvature is approximated numerically for $\rho^-/\rho^+ = 10, \mathrm{We} = 1$. For the verification test case of the two-phase momentum advection problem, $\rho^-/\rho^+ = 10^6$ is used without surface tension and viscous forces and qualitative results show slight deformations of the interface shape, the L_∞ norm of the velocity error is not reported. With enabled surface tension and viscous forces and exact curvature prescribed, and density ratios $\rho^-/\rho^+ = 1, 1000$, the velocity error in the L_∞ norm lies within $[10^{-3}, 10^{-2}]$.

Manik et al. [31], similarly to [30], attempt to enforce numerical consistency by applying the similar discretization scheme on the conservative form of the volume fraction advection equation and the momentum conservation equation. Manik et al. [31] are using a collocated unstructured Finite Volume method for the equation discretization and the CUBISTA scheme (Alves et al. [32]) to discretize convective terms. The verification of the numerical consistency for the two-phase momentum advection is done using the droplet translation case of Bussmann et al. [16] and density ratios $\rho^-/\rho^+ = 10^3, 10^6$, that demonstrates qualitative improvement compared to a naive discretization of the momentum convective term with the upwind method. The qualitative evaluation is based on the shape of the droplet, given by the 0.5 iso-surface of the volume fraction. Although the proposed method demonstrates improvement w.r.t. an obviously inconsistent approach, some shape deformation is still visible, so one can conclude that $L_\infty(\mathbf{v}) \neq 0$ and some non-zero velocities are still generated.

A recent second-order accurate LS method is proposed by Nangia et al. [4], extending the work from Ghods and Herrmann [3] that is first-order accurate. Similar to the method proposed by Ghods and Herrmann [3], an additional mass conservation equation is solved, and the identical mass flux is used for both mass and momentum transport. Two techniques are employed: one is the third-order accurate Koren's limited CUI, which is modified to consistently discretize the convective term of both mass and momentum equation. This scheme satisfies the convection-boundedness criterion (CBC) and is total variation diminishing (TVD). The second technique is the solution of an update equation for the face-centred densities. In this step, a third-order accurate strong stability preserving Runge-Kutta (SSP-RK3) scheme is used for time integration. The update is performed in every fixpoint iteration, and the updated face-centered density is then employed to solve the discretized momentum equation.

Zuzio et al. [7] also follow Ghods and Herrmann [3] by solving an auxiliary continuity equation for increasing the numerical consistency in discretizing the two-phase momentum convection

term. Their Consistent Mass-Momentum (CMOM) transport method utilizes a staggered Cartesian variable arrangement and utilizes the two-phase incompressible Navier-Stokes equations in the conservative form, solved using Chorin's projection method [33] together with the CLSVOF method for tracking the fluid interface. The solution of the auxiliary density equation requires the evaluation of staggered (face-centered) densities, by constructing staggered control volumes, and evaluating the densities using sub-grid quadtree (octree in 3D) refinement and intersection with the PLIC interfaces. This aspect of CMOM shows the importance of evaluating the densities at face-centeres that are required for the solution of the auxiliary continuity equation. Momentum flux reconstruction scales the fluxed phase-specific volume from the VOF method. Finally, the two-phase momentum is advected in the staggered cells, and scaled with the corresponding density to obtain velocity components in all spatial directions. Zuzio et al. [7] demonstrate significant improvements in numerical stability in a very detailed way, reporting shape, position and kinetic energy errors for canonical verification and validation cases. The kinetic energy for the dense translating droplet [16] with a density ratio of 10^6 is reported, and CMOM recovers a numerically stable solution.

Arrufat et al. [34] consider the conservative form of the advection equation of a discontinuous property to enforce numerical consistency of the advected two-phase momentum, using face averages that are derived by integrating the advection equation in space and time. Since the discontinuity of the property introduced by the interface complicates the evaluation of the face averages, two additional equations are introduced, one for each phase. The method is derived for the MAC staggered variable arrangement. Results demonstrate a numerically stable droplet shape when it is advected with a constant velocity, however, the authors consider this case to only test the consistency of the implementation and not the numerical consistency of the method - we consider it important for both - so the results are not quantified in terms of kinetic energy or L_∞ velocity errors. Still, the method shows significant improvements for realistic multiphase flows with high density ratios.

The high-density ratio is also challenging for other numerical methods for two-phase flows, like the phase-field and lattice Boltzmann. The corresponding surveys are beyond the scope of this work, more details can be found in [35, 36, 37, 38, 39, 40]. Contrary to the numerical two-phase methods mentioned so far, the difficulties with high density ratios are far less pronounced for Front Tracking methods [41] because the marker field (phase-indicator) is not as sharp as in the unstructured Volume-of-Fluid method [42] and the unstructured Level Set / Front Tracking method [1, 2].

The methods of Bussmann et al. [16], Ghods and Herrmann [3], Patel and Natarajan [30], Manik et al. [31] utilize the unstructured Finite Volume equation discretization, other above-mentioned methods utilize a staggered variable arrangement that is not applicable to unstructured meshes. Compared to contemporary collocated Finite Volume methods, our proposed ρLENT method achieves the numerical consistency in the two-phase momentum advection exactly. We derive the requirement for the auxiliary mass conservation equation introduced by Ghods and Herrmann [3], and derive the requirement for the face-centered (flux) density from the mass conservation principle. Compared to a similar observation by [34], we avoid the integration in time that complicates the evaluation of face-centered quantities, as demonstrated in detail below. Although hybrid Level Set / Front Tracking LENT method [1] is used for interface capturing, the ρLENT solution algorithm can be used with other interface capturing methods, where there is a discrepancy in the evaluation of the collocated density.

We utilize a collocated unstructured Finite Volume discretization because it is ideal for geometrically complex domains. At its core, the proposed unstructured collocated finite-volume ρLENT **LE**vel set / fro**NT** tracking method geometrically approximates the face-centered density in the mass flux and implicitly discretizes the two-phase momentum convective term, thus avoiding the

interpolation of face-centered densities and the CFL stability criterion introduced in [16].

2. Mathematical model

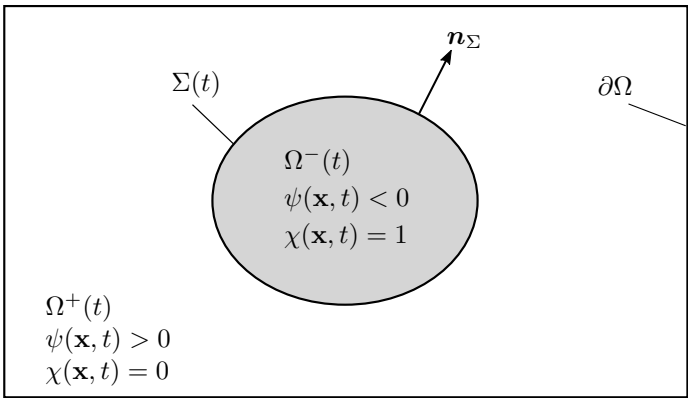

Figure 1: The domain Ω, split by the fluid interface $\Sigma(t)$ into two sub-domains $\Omega^{\pm}$.

As shown in fig. 1, the overall flow domain $\Omega \subset \mathbb{R}^3$ is filled with two phases which occupy subdomains $\Omega^-(t)$ and $\Omega^+(t)$, such that $\Omega = \Omega^+(t) \cup \Omega^-(t) \cup \Sigma(t)$. The unit normal vector $\boldsymbol{n}_\Sigma$ of the interface $\Sigma(t)$ is oriented outwards for the subdomain $\Omega^-(t)$. These two phases have different material properties that change sharply across the interface $\Sigma(t)$, separating the two subdomains. To identify the phase at a particular location $\mathbf{x}$ and time t, the phase indicator is utilized and defined as

$$\chi(\mathbf{x},t) := \begin{cases} 1, & \mathbf{x} \in \Omega^-(t), \\ 0, & \mathbf{x} \in \Omega^+(t). \end{cases} \tag{1}$$

In this work, a single-field formulation of governing equations is used to model incompressible two-phase flows without phase-change. Constant density and dynamic viscosity of the two phases, namely ρ^-, ρ^+ and μ^-, μ^+ are combined into single-fields using the phase indicator:

$$\rho(\mathbf{x},t) = \chi(\mathbf{x},t)\rho^- + (1-\chi(\mathbf{x},t))\rho^+ = (\rho^- - \rho^+)\chi(\mathbf{x},t) + \rho^+, \tag{2}$$

$$\mu(\mathbf{x},t) = \chi(\mathbf{x},t)\mu^- + (1-\chi(\mathbf{x},t))\mu^+ = (\mu^- - \mu^+)\chi(\mathbf{x},t) + \mu^+, \tag{3}$$

and used in the Navier-Stokes equations in the single-field formulation model the incompressible two-phase flow,

$$\nabla \cdot \mathbf{v} = 0, \tag{4}$$

$$\partial_t(\rho\mathbf{v}) + \nabla \cdot (\rho\mathbf{v} \otimes \mathbf{v}) = -\nabla P + \rho\mathbf{g} + \nabla \cdot \left(\mu\left(\nabla\mathbf{v} + (\nabla\mathbf{v})^T\right)\right) + \mathbf{f}_\Sigma. \tag{5}$$

With $\mathbf{x}$ as the position vector and constant gravitational acceleration $\mathbf{g}$, we can write

$$\nabla(\rho\mathbf{g}\cdot\mathbf{x}) = (\mathbf{g}\cdot\mathbf{x})\nabla\rho + \rho\mathbf{g}\cdot\nabla\mathbf{x} = (\mathbf{g}\cdot\mathbf{x})\nabla\rho + \rho\mathbf{g}, \tag{6}$$

since $\nabla\mathbf{x} = \mathbf{I}$ ($\mathbf{I}$ is the identity matrix). We rearrange $-\nabla P + \rho\mathbf{g}$ on the r.h.s. of eq. (5) using eq. (6)

$$-\nabla P + \rho\mathbf{g} = -\nabla P + \nabla(\rho\mathbf{g}\cdot\mathbf{x}) - (\mathbf{g}\cdot\mathbf{x})\nabla\rho = -\nabla(P - \rho\mathbf{g}\cdot\mathbf{x}) - (\mathbf{g}\cdot\mathbf{x})\nabla\rho, \tag{7}$$

and defining the dynamic pressure as $p := P - \rho \mathbf{g} \cdot \mathbf{x}$ results in

$$\partial_t(\rho \mathbf{v}) + \nabla \cdot (\rho \mathbf{v} \otimes \mathbf{v}) = -\nabla p - (\mathbf{g} \cdot \mathbf{x}) \nabla \rho + \nabla \cdot \left(\mu \left(\nabla \mathbf{v} + (\nabla \mathbf{v})^T \right) \right) + \mathbf{f}_\Sigma. \tag{8}$$

The surface tension force per unit volume $\mathbf{f}_\Sigma$ exerts a force on the interface $\Sigma(t)$ and is modeled using a CSF (Continuum Surface Force) model [43]

$$\mathbf{f}_\Sigma = \sigma \kappa \mathbf{n}_\Sigma \delta_\Sigma \tag{9}$$

with a constant surface tension coefficient σ, κ as twice the local mean curvature of $\Sigma(t)$, and δ_Σ as the interface Dirac distribution.

3. A solution algorithm for two-phase flows with high density ratios using the collocated unstructured Finite Volume method

The volume fraction $\alpha(\mathbf{x}, t)$ is defined as a volumetric average of the phase indicator$\chi(\mathbf{x}, t)$ over a fixed control volume Ω_c, i.e.

$$\alpha_c(t) := \frac{1}{|\Omega_c|} \int_{\Omega_c} \chi(\mathbf{x}, t) \, dV, \tag{10}$$

and in the equation discretization using the unstructured Finite Volume method, Ω_c corresponds to the finite volume (mesh cell), generating a discrete field of volume fractions $\{\alpha_c\}_{c \in C}$. For simplicity, we denote both $\{\alpha_c\}_{c \in C}$ and α_c with α_c and use the plural "volume fractions" when discussing $\{\alpha_c\}_{c \in C}$ and singular "volume fraction" when discussing α_c in the text below. The volume fractions $\alpha_c(t)$ are approximated from the geometrical approximation of the fluid interface $\Sigma(t)$, the so-called Front $\tilde{\Sigma}(t) \approx \Sigma(t)$, that is advected using the flow velocity $\mathbf{v}(t)$ by unstructured finite-volume Level Set / Front Tracking (LENT) method [1]. The LENT method geometrically computes signed distances $\psi(\mathbf{x}, t)$, positive in the direction of $\mathbf{n}_\Sigma$ (cf. fig. 1), details are given in [1, 2, 44].

The collocated unstructured Finite Volume method [45, 46, 47], which is implemented in the OpenFOAM open-source software [48, 49, 50], associates with the centroid of the finite volume Ω_c the density

$$\rho_c(t) = (\rho^- - \rho^+) \alpha_c(t) + \rho^+, \tag{11}$$

and the viscosity

$$\mu_c(t) = (\mu^- - \mu^+) \alpha_c(t) + \mu^+. \tag{12}$$

Equations (11) and (12) are used in a collocated FV discretization of eq. (8). The surface tension force given by eq. (9) is approximated as

$$\mathbf{f}_{\Sigma,c} \approx \sigma \kappa_c \nabla \alpha_c, \tag{13}$$

where cell-centered curvature κ_c is calculated using $\nabla \cdot (\frac{\nabla \psi}{|\nabla \psi|})$, and ψ is the geometrically computed distance from the Front [1]. The cell curvature κ_c is propagated as a constant in the interface-normal direction using a so-called spherical correction. Details on curvature calculation are given in [2]. The term $\nabla \alpha_c$ denotes a discrete finite volume gradient of the volume fraction used to approximate the interface Dirac distribution.

3.1. The unstructured Finite Volume Hybrid Level Set / Front Tracking method

Hybrid multiphase flow simulation methods combine the sub-algorithms of the Front Tracking, Level Set, or Volume-of-Fluid methods to achieve better overall results. The structured Hybrid Level Set / Front Tracking method ([51, 52, 53, 41, 54]) has demonstrated remarkable capabilities for simulating a wide range of multiphase flows. The unstructured Level Set / Front Tracking method - the LENT method [1, 2, 44] - shows promising computational efficiency and accuracy for surface tension driven flows on unstructured meshes.

However, LENT method in its existing form cannot handle two-phase flows with strongly different densities. Cell-centered volume fractions $\alpha_c(t)$ are computed from signed distances $\psi_c(t)$, that are computed geometrically from the Front $\tilde{\Sigma}(T) \approx \Sigma(t)$: a triangular surface mesh that approximates the fluid interface $\Sigma(t)$. This geometrical calculation of α_c from $\tilde{\Sigma}(t)$ and, subsequently, the calculation of ρ_c from α_c by eq. (11), together with the interpolation of the face-centered density in the mass flux of the discretized convective term from eq. (8), introduces an inconsistency that we describe in detail and address below.

3.2. Numerical consistency of the single-field conservative two-phase momentum convection term

As outlined in the introduction section 1, many authors have addressed numerical instabilities in various discretizations and two-phase flow methods arising from high-density ratios. Here, we provide a detailed analysis of the inconsistencies that lead to numerical instabilities by studying the relationships between mass conservation, phase indicator function conservation, and momentum convection. It turns out that the conservative formulation of conservation equations permits us to precisely define equalities that must hold in the mathematical model and its discretization to achieve consistency in the equation system and prevent numerical instabilities.

Bussmann et al. [16] were the first to consider the problem of numerical consistency of the two-phase momentum convective term in the setting of the collocated unstructured Finite Volume method. We expand on their work by improving the accuracy of the face-centered density evaluation and employing a solution algorithm that allows for an implicit discretization of the convective term, thus removing the CFL condition. We discretize the two-phase momentum convection term from eq. (8) using the collocated unstructured finite volume method (FVM) [45, 55, 56] as

$$\int_{\Omega_c} \nabla \cdot (\rho \mathbf{v} \otimes \mathbf{v})\, dV = \int_{\partial\Omega_c} (\rho \mathbf{v} \otimes \mathbf{v}) \cdot \mathbf{n}\, ds = \sum_{f \in F_c} \rho_f F_f \mathbf{v}_f + O_{\rho\mathbf{v},con}(h^2). \tag{14}$$

The second-order discretization error is denoted as $O_{\rho\mathbf{v},con}(h^2)$, with the $\rho\mathbf{v}$ subscript indicating the equation ($\rho\mathbf{v}$ for momentum eq. 8), *con* subscript the convective term of the equation, and h the discretization length.The convective term in eq. (14) has been linearized with respect to the solution variable $\mathbf{v}$ in order to obtain a linear equation system. Here, ρ_f represents the face-center density, and F_f represents the linearized volumetric flux. Details on the flux linearization and temporal integration are given in section 3.3, here we first focus on the spatial discretization.

The discretization 14 requires a mass flux $\rho_f F_f$. The volume fraction conservation and the conservation of mass are equivalent if both phases are incompressible. To show this, we write the mass conservation equation in conservative form in a fixed (time-independent) control volume $\Omega_c \neq \Omega_c(t)$ as

$$\partial_t \int_{\Omega_c} \rho\, dV = -\int_{\partial\Omega_c} \rho \mathbf{v} \cdot \mathbf{n}\, dS. \tag{15}$$

Applying eq. (2) and eq. (4) to eq. (15) leads to

$$(\rho^- - \rho^+)\partial_t \int_{\Omega_c} \chi \, dV = -(\rho^- - \rho^+) \int_{\partial\Omega_c} \chi \mathbf{v} \cdot \mathbf{n} \, dS - \rho^+ \int_{\partial\Omega_c} \mathbf{v} \cdot n \, dS, \tag{16}$$

with $\int_{\partial\Omega_c} \mathbf{v} \cdot n \, dS = \int_{\Omega_c} \nabla \cdot \mathbf{v} \, dV = 0$ because of eq. (4). Dividing eq. (16) by $|\Omega_c|$, and using the volume fraction definition 10 leads to

$$(\rho^- - \rho^+)\partial_t \alpha_c(t) = -(\rho^- - \rho^+)\frac{1}{|\Omega_c|} \int_{\partial\Omega_c} \chi \mathbf{v} \cdot \mathbf{n} \, dS. \tag{17}$$

The eq. (15) implies

$$\partial_t \rho_c(t) = -\frac{1}{|\Omega_c|} \int_{\partial\Omega_c} \rho \mathbf{v} \cdot \mathbf{n} \, dS. \tag{18}$$

An important equality arises from eqs. (15), (17) and (18), namely

$$\partial_t \rho_c(t) = -\frac{1}{|\Omega_c|} \int_{\Omega_c} \rho \mathbf{v} \cdot \mathbf{n} \, dV = (\rho^- - \rho^+)\partial_t \alpha_c(t) = -(\rho^- - \rho^+)\frac{1}{|\Omega_c|} \int_{\partial\Omega_c} \chi \mathbf{v} \cdot \mathbf{n} \, dS. \tag{19}$$

Selecting $\partial_t \rho_c(t) = (\rho^- - \rho^+)\partial_t \alpha_c(t)$ from eq. (19), and integrating over the time interval $[t^n, t^{n+1}]$ leads to

$$\rho_c^{n+1} = (\rho^- - \rho^+)\alpha_c^{n+1} + \rho_c^n - (\rho^- - \rho^+)\alpha_c^n, \tag{20}$$

and applying eq. (11) at t^n to eq. (20) leads to

$$\rho_c^{n+1} = (\rho^- - \rho^+)\alpha_c^{n+1} + \rho^+, \tag{21}$$

which is eq. (11) at t^{n+1}. Note that the time integration is exact because of the fundamental theorem of calculus. The equality $\partial_t \rho_c(t) = (\rho^- - \rho^+)\partial_t \alpha_c(t)$ from eq. (19) can lead to a false conclusion of consistency of the two-phase momentum convection. If other equalities from eq. (19) are not upheld, e.g. when the method that advects the phase indicator α_c does not rely on phase-specific fluxes (cf. [42] for a recent review), inconsistencies arise.

Since unstructured finite volumes are bounded by faces S_f, we can rewrite

$$\frac{1}{|\Omega_c|} \int_{\Omega_c} \rho \mathbf{v} \cdot \mathbf{n} \, dV = (\rho^- - \rho^+)\frac{1}{|\Omega_c|} \int_{\partial\Omega_c} \chi \mathbf{v} \cdot \mathbf{n} \, dS$$

from eq. (19) as

$$\sum_{f \in F_c} \int_{S_f} \rho \mathbf{v} \cdot \mathbf{n} \, dS = (\rho^- - \rho^+) \sum_{f \in F_c} \int_{S_f} \chi \mathbf{v} \cdot \mathbf{n} \, dS, \tag{22}$$

and discretize it further using second-order-accurate face-averages, resulting in

$$\begin{aligned} \sum_{f \in F_c} \rho_f F_f + O_{\rho,con}(h^2) &= \sum_{f \in F_c} (\rho^- - \rho^+)\frac{F_f}{|\mathbf{S}_f|} \int_{S_f} \chi dS + O_{\alpha,con}(h^2) \\ &= \sum_{f \in F_c} (\rho^- - \rho^+) F_f \alpha_f + O_{\alpha,con}(h^2), \end{aligned} \tag{23}$$

with $\phi_f := \frac{1}{|S_f|}\int_{S_f} \phi\, dS$ defining the face-average associated to the centroid of each face S_f. In eq. (23), $F_f := \mathbf{v}_f \cdot \mathbf{S}_f$ is the linearized volumetric flux given by the velocity $\mathbf{v}$ from the discretized single-field Navier-Stokes equations eqs. (4) and (8). Equation (23) reveals an important fact: the mass flux $\rho_f F_f$ - necessary for the discretization of the two-phase momentum convective term 14 - must be linearly proportional to the phase-specific volumetric flux $F_f \alpha_f$ used to advect the phase indicator α_c, with $(\rho^- - \rho^+)$ as the proportionality coefficient. This consistency is not ensured by any two-phase flow simulation method that does not solve an advection equation for the volume fractions using a flux-based discretization method.

We extend the unstructured Level Set / Front Tracking LENT method [1, 2, 44] to ensure that the condition from eq. (23) is upheld. Before describing the numerical method in detail, we discuss a verification case of a droplet advected in a constant velocity field.

3.2.1. Verification case: droplet translating with constant velocity

We consider the Euler explicit collocated unstructured FV discretization of eq. (15), i.e.,

$$\rho_c^{n+1} = \rho_c^n - \frac{\Delta t}{|\Omega_c|}\sum_{f\in F_c} \rho_f^n F_f^n. \tag{24}$$

The two-phase momentum advection is modeled using eq. (8) with a prescribed initial constant velocity and without forces on the r.h.s, namely

$$\partial_t(\rho\mathbf{v}) + \nabla\cdot(\rho\mathbf{v}\otimes\mathbf{v}) = 0. \tag{25}$$

Without forces on the r.h.s. of eq. (25), the initial constant velocity should remain spatially constant. Therefore, a numerically consistent unstructured collocated FVM discretization of the two-phase momentum convection equation (eq. (25)) must ensure that no artificial acceleration or deceleration occurs. For example, just like eq. (24), the Euler explicit discretization of eq. (25) is

$$\rho_c^{n+1}\mathbf{v}_c^{n+1} = \rho_c^n\mathbf{v}_c^n - \frac{\Delta t}{|\Omega_c|}\sum_{f\in F_c} \rho_f^n F_f^n \mathbf{v}_f^n. \tag{26}$$

Given a consistent discretization, the velocity field remains spatially constant, so

$$\mathbf{v}_f^n = \mathbf{v}_c^n, \tag{27}$$

which is, of course, ensured for the initial spatially constant velocity ($\mathbf{v}_f^0 = \mathbf{v}_c^0$). Equation (27), applied to eq. (26), results in

$$\rho_c^{n+1}\mathbf{v}_c^{n+1} = \mathbf{v}_c^n\left(\rho_c^n - \frac{\Delta t}{|\Omega_c|}\sum_{f\in F_c} \rho_f^n F_f^n\right), \tag{28}$$

and dividing by ρ_c^{n+1} finally gives

$$\mathbf{v}_c^{n+1} = \frac{\mathbf{v}_c^n\left(\rho_c^n - \frac{\Delta t}{|\Omega_c|}\sum_{f\in F_c} \rho_f^n F_f^n\right)}{\rho_c^{n+1}}. \tag{29}$$

As there are no forces on the r.h.s. of eq. (25), the velocity should not be changed simply by advecting the two-phase momentum, i.e.

$$\mathbf{v}_c^{n+1} = \mathbf{v}_c^n, \tag{30}$$

and this condition is ensured in eq. (29) if

$$\frac{\rho_c^n - \frac{\Delta t}{|\Omega_c|} \sum_{f \in F_c} \rho_f^n F_f^n}{\rho_c^{n+1}} = 1, \tag{31}$$

which is equivalent to eq. (24): the Euler explicit discretization of the mass conservation equation. Consequently, a numerically consistent discretization of the momentum convection equation in this verification case requires the new cell-centered density ρ_c^{n+1} to be computed by solving a mass conservation equation.

Modern unstructured geometric flux-based Volume-of-Fluid (VOF) methods ([57, 27, 58, 59], see [60] for a recent review) potentially ensure this property, since they solve the conservative formulation of the volume fraction advection equation [42] for α_c^{n+1} by computing phase-specific fluxed volumes, scale the phase-specific fluxed volumes to compute the mass flux, and use the cell-centered volume fraction α_c^{n+1} to compute ρ_c^{n+1} with eq. (11). However, the temporal discretization scheme used in the momentum equation for the convective term must be consistent with the integration of the fluxed phase-specific volumes, used to obtain α_c^{n+1}. Even if the mass flux can be computed by scaling the phase-specific fluxed volumes with δt, any difference between the temporal integration schemes used for the volume fraction and momentum equations, or any flux limiting in the momentum equation, cause inconsistencies. Additionally, the $\alpha_c^{n+1} \in [0, 1]$ must hold near machine epsilon. Any correction to α_c^{n+1} performed after the numerical solution of the volume fraction advection equation, that bounds α_c^{n+1} within $[0, 1]$, results in a discrepancy between ρ_c^{n+1} computed using the mass flux that gives unbounded α_c^{n+1}, and the ρ_c^{n+1} computed from the a-posteriori bounded α_c^{n+1} using eq. (11).

It is important to note that if the pressure gradient is included on the r.h.s of eq. (25), any error in $\mathbf{v}_c^{n+1}$ will result in non-zero source terms on the r.h.s. of the resulting pressure equation, in the $p - \mathbf{v}$ coupling algorithm. Since the pressure gradient enforces $\nabla \cdot \mathbf{v} = 0$ ($\sum_{f \in F_c} F_f = 0$ on the discrete level), this results in artificial velocities similar to parasitic currents caused by the surface tension force.

Bussmann et al. [16] have utilized the consistency of the Volume-of-Fluid method and the availability of phase-specific volumetric fluxes in the VOF method to first solve eq. (25) explicitly in the first step, followed by the second step that includes volume and surface forces. The approach from Bussmann et al. [16] cannot be applied without modifications to the Level Set method, the Front Tracking method, their hybrids, or any other collocated FV two-phase flow simulation method that does not rely on phase-specific volumetric fluxes to discretely advect volume fractions. If the phase-specific volumetric fluxes (or volumes) are not calculated by the method, they cannot be used to construct a consistent mass flux. The solution algorithm for high density ratios that we propose avoids the CFL condition imposed by Bussmann et al. [16] and increases the accuracy of the face-centered density ρ_f required by the mass flux, and it is applicable to any multiphase flow simulation method that utilizes the single-field formulation of the Navier-Stokes equations.

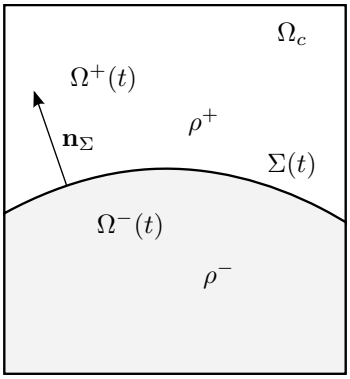

Figure 2: A two-phase fixed control volume Ω_c separated by the interface $\Sigma(t)$.

3.3. A semi-implicit solution algorithm for high-density ratios

Section 3.2 provides the formal reasoning behind solving the mass conservation equation (or its equivalent) for ρ_c^{n+1}. Since Ghods and Herrmann [3] introduced what we call an "auxiliary" mass conservation equation, other researchers have adopted this approach, with the main difference in the way the face-centered (mass flux) density ρ_f is evaluated both in the discretized mass conservation equation (eq. (15)) and the discretized momentum equation (eq. (8)).

The condition given by eq. (31), derived from eqs. (29) and (30) can be fulfilled only if the same face-centered (mass flux) density is used when discretizing the auxiliary mass conservation and momentum equations. Going one step further, the volumetric flux F_f must also be the same in the discretized auxiliary mass conservation and momentum equations. Put together, the mass flux in the auxiliary discretized mass conservation equation must be equal to the mass flux in the discretized momentum conservation equation: this is the requirement for the mass flux consistency, mentioned throughout the literature.

It is relevant to point out that the same model for the single-field density given by eq. (11) is used throughout the literature. The basis of this model is mass conservation, and this fundamental principle further leads to an interesting conclusion regarding the evaluation of the face-centered (mass flux) density ρ_f in the discretized mass and momentum conservation equations. The face centered density is evaluated differently throughout scientific publications reviewed in section 1, and here we show that there is a strict relationship between the phase indicator and the face centered density ρ_f.

Consider the fixed control volume Ω_c in fig. 2, that is separated by the fluid interface $\Sigma(t)$ into two parts, occupied by fluids $\Omega^{\mp}(t)$. The single-field density model given by eq. (2) is adopted in every publication reviewed in section 1, an in the rest of the scientific literature on two-phase flow simulations. The mass conservation principle together with the single-field density model (eq. (2)) give

$$\frac{d}{dt}\int_{\Omega_c}\rho\,dV = -\int_{\partial\Omega_c}\rho\mathbf{v}\cdot\mathbf{n}dS = -\int_{\partial\Omega_c}[\rho^-\chi+\rho^+(1-\chi)]\mathbf{v}\cdot\mathbf{n}\,dS. \tag{32}$$

The equality of surface integrals in eq. (32),

$$\int_{\partial\Omega_c}\rho\mathbf{v}\cdot\mathbf{n}dS = \int_{\partial\Omega_c}[\rho^-\chi+\rho^+(1-\chi)]\mathbf{v}\cdot\mathbf{n}\,dS,$$

demonstrates that the mass flux of the single-field density over $\partial\Omega_c$ is determined by the constant densities $\rho^{\mp}$ and the phase indicator given by eq. (1), if eq. (2) is used to model the single-field density. In other words, the single-field density at $\partial\Omega_c$ should be computed using the phase indicator as done on the r.h.s. of eq. (32), otherwise the mass conservation of the single-field density model given by eq. (2) will not be upheld. This relevant condition transfers to the discrete level, leading to an interesting consequence for the computation of the face-centered (mass flux) density, that has so far been computed in many ways throughout the literature.

Specifically, when the surface integrals in eq. (32) are discretized using the unstructured collocated finite volume method,

$$\begin{aligned}
\sum_{f\in F_c} \rho_f F_f &= \sum_{f\in F_c} \left[\rho^- \left(\int_{S_f} \chi \, dS \right) \mathbf{v}_f \cdot \hat{\mathbf{S}}_f + \rho^+ \left(\int_{S_f} dS \right) \mathbf{v}_f \cdot \hat{\mathbf{S}}_f - \rho^+ \left(\int_{S_f} \chi \, dS \right) \mathbf{v}_f \cdot \hat{\mathbf{S}}_f \right] \\
&= \sum_{f\in F_c} \left[\rho^- \frac{\|\mathbf{S}_f\|}{\|\mathbf{S}_f\|} \left(\int_{S_f} \chi \, dS \right) \mathbf{v}_f \cdot \hat{\mathbf{S}}_f + \rho^+ \left(\int_{S_f} dS \right) \mathbf{v}_f \cdot \hat{\mathbf{S}}_f \right. \\
&\left. -\rho^+ \frac{\|\mathbf{S}_f\|}{\|\mathbf{S}_f\|} \left(\int_{S_f} \chi \, dS \right) \mathbf{v}_f \cdot \hat{\mathbf{S}}_f \right] \\
&= \sum_{f\in F_c} \left[\rho^- \alpha_f + \rho^+ (1-\alpha_f) \right] F_f,
\end{aligned} \tag{33}$$

where

$$\alpha_f := \frac{1}{|S_f|} \int_{S_f} \chi \, dS \equiv \frac{|\Omega^-(t) \cap S_f|}{|S_f|} \tag{34}$$

is the area fraction of the face $S_f \subset \partial\Omega_c$, i.e. the ratio of the area of S_f submerged in $\Omega^-(t)$, and the total face-area $|S_f|$. Further, $\|\mathbf{S}_f\| \equiv |S_f|$, and F_f is the volumetric flux in eq. (33).

An important consequence of eq. (33) is the requirement for the evaluation of the face-centered (mass flux) density, necessary for ensuring the numerical consistency of the single-field two-phase momentum convection. Equation (33) requires all methods[4] that define ρ using eq. (11) to either compute ρ_f using the area fractions or $\int_{S_f} \chi \, dS$ from eq. (33), or to achieve this equivalently when computing ρ_c^{n+1} from the advected volume fractions α_c^{n+1}, which is possible for the flux-based VOF methods [60].

Another important realization is that eq. (33) is valid at any time t - which is very relevant for the semi-implicit discretization developed within the ρLENT method, that applies eq. (33) at t^{n+1}.

Any simulation method that relies on the collocated unstructured FV discretization of single-field two-phase Navier-Stokes equations, but does not advect the phase indicator by solving an advection equation using phase-specific volumetric fluxes, does not provide the phase-specific volumetric fluxes for the approximation of the mass fluxes needed to ensure the consistency of the two-phase momentum transport. This, however, does not infer that eq. (33) cannot be applied. The idea of using an auxiliary mass conservation equation introduced by [3], made into a formal requirement by eqs. (29) and (30), allows the use of eq. (33): α_f can be computed regardless of the approximation of the fluid interface $\Sigma(t)$ and the method used to advect it.

[4] All two-phase flow simulation methods encountered by the authors use eq. (11).

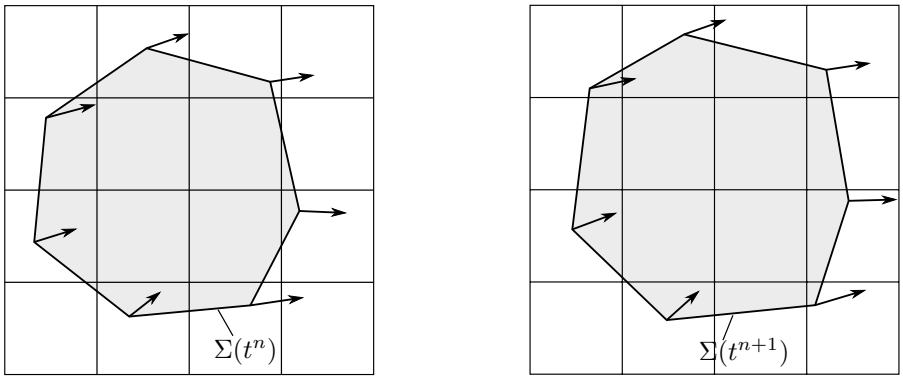

(a) Interface Σ at t^n and t^{n+1} and the respective $\Omega^-(t^n)$ and $\Omega^-(t^{n+1})$ in gray color, used to compute α_c^n and α_c^{n+1}, that are further used to compute ρ_c^n and ρ_c^{n+1} in an inconsistent way.

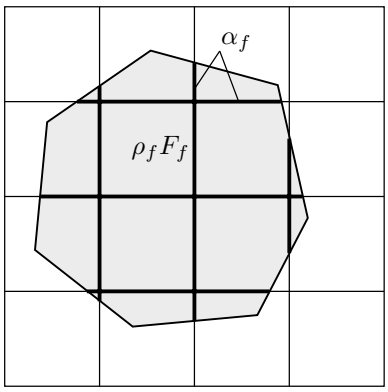

(b) Interface at $\Sigma(t^{n+1})$ used to compute α_f^{n+1}, then ρ_f^{n+1} and finally ρ_c^{n+1} in a consistent way, by solving a mass conservation equation.

Figure 3: Updating the face-centered (mass flux) density in the ρLENT method.

Similar to other contemporary methods, the ρLENT method also first advects the interface using the velocity from the previous time step as shown in the left image of fig. 3a, resulting in the new position of the interface shown in the right image in fig. 3a, that is then used to geometrically calculate the face-centered density ρ_f^{n+1}, by calculating area fractions α_f^{n+1} from the interface approximation, as shown in fig. 3b. The face-centered density ρ_f^{n+1} and the volumetric flux F_f^o are then used to update the cell-centered density ρ_c^{n+1} by solving a mass conservation equation. The index o in the volumetric flux refers to the linearization of the convective term in the momentum equation. The same mass flux $\rho_f^{n+1}F_f^o$ is used in the implicitly discretized momentum conservation equation. The pressure-velocity coupling algorithm iterates the linearized volumetric flux F_f^o to F_f^{n+1}. Finally, the cell-centered velocity $\mathbf{v}_c^{n+1}$ is obtained, which is used to evolve the fluid interface in the next time step, from t^{n+1} to t^{n+2}. At this point, the numerically consistent cell-centered

density ρ_c^{n+1} has served its purpose and is reset according to eq. (11), using α_c approximated from signed distances [2], to make it consistent again with the fluid interface approximation.

Any two-phase flow simulation method has the possibility to compute the face-centered density $\rho_f(t)$ from the interface approximation in some way. The ρLENT method computes the face-centered density $\rho_f(t)$ by computing the face area fraction $\alpha_f(t)$ (short: area fraction) of the face S_f, submerged in the phase $\Omega^-(t)$. The calculation of α_f uses signed distances available in the unstructured LENT [1, 2]. Any two-phase flow simulation method that utilises the collocated FV method for discretizing single-field Navier-Stokes equations can be adapted as described above to geometrically approximate the area fraction α_f thus avoiding erroneous interpolation of fields that abruptly change in the interface-normal direction.

In the original Front-Tracking method, the density is updated utilizing the new position of marker points (the approximated interface) [61]. After the velocity field in the current step is computed, the position of marker points in the new time step can be updated immediately by

$$\mathbf{x}_p^{n+1} = \mathbf{x}_p^n + \Delta t\, \mathbf{v}_p^n, \tag{35}$$

where $\mathbf{x}_p$,$\mathbf{v}_p$ indicate the position and interpolated velocity of marker points respectively, and Δt is the time step length. The advection of marker points along Lagrangian trajectories eventually corrupts the triangular mesh, leading to discrepancies in the ratios of triangular angles and areas and self-intersections of the triangular mesh. The original Front Tracking method [62] deals with this by redistributing marker points based on quality criteria imposed on the triangular mesh, which involves manipulating the connectivity of the triangular mesh.

Contrary to original Front Tracking [62], the LENT method reuses the principles from LCRM / LFRM methods [51, 52, 41, 54] and reconstructs the interface using an iso-surface reconstruction algorithm. The iso-surface reconstruction does not add/delete marker points locally by changing the connectivity of the triangular surface mesh; it reconstructs the entire interface in the solution domain as an iso-surface. Following the strategy from LCRM / LFRM, the physics of the problem determines the iso-surface reconstruction frequency. The LENT method uses the marching tetrahedra [63] algorithm to enable the iso-surface reconstruction on unstructured meshes.

Once the marker points are advected and redistributed, the cell density is updated depending on $\mathbf{x}_p^{n+1}$, namely

$$\rho^{n+1} = \rho(\mathbf{x}_p^{n+1}). \tag{36}$$

The face-centered density used for the mass flux is then interpolated by the LENT method from densities of two adjacent cells. Contrary to LENT, the face-centered density is updated by ρLENT using the phase indicator approximated at each cell-face by an area fraction. A 2D interface is depicted in fig. 3b, where α_f^{n+1} is the area fraction at t^{n+1}: the ratio of the cell-face area submerged in the phase $\tilde{\Omega}^-(t^{n+1}) \approx \Omega^-(t^{n+1})$, and the total face area $|S_f|$. More precisely, the area fraction α_f^{n+1} is computed by the ρLENT method using a second-order accurate approximation from signed distances [64], used in [2] to approximate the volume fraction α_c (see eq. (10)). The Level Set component of the LENT method [1] calculates signed distances from the triangular surface mesh that approximates the interface $\tilde{\Sigma}(t^{n+1}) \approx \Sigma(t^{n+1}) := \partial\tilde{\Omega}^-(t^{n+1})$. With the narrow band approach from [1], the signed distances can be computed efficiently at any point in a close vicinity of $\tilde{\Sigma}(t)$. The original LENT method [1] computes signed distances at cell-centers and cell corner-points, and the proposed ρLENT additionally computes signed distances at face centers. Each face S_f is triangulated using its centroid $\mathbf{x}_f$, as shown in fig. 4. The face centroid $\mathbf{x}_f$, together with the two successive cell-corner points that belong to the face S_f, $\mathbf{x}_{f,i}$, $\mathbf{x}_{f,i+1}$, forms a triangle $(\mathbf{x}_f, \mathbf{x}_{f,i}, \mathbf{x}_{f,i+1})$. Face-triangles

may be partially submerged in the phase $\tilde{\Omega}^-(t^{n+1})$, in which case the submerged area of the triangle is computed using the nearest signed distances to $\tilde{\Sigma}(t^{n+1})$ from the triangle points $(\mathbf{x}_f, \mathbf{x}_{f,i}, \mathbf{x}_{f,i+1})$, namely $(\psi_f, \psi_{f,i}, \psi_{f,i+1})$, as shown in fig. 4. The second-order approximation developed in [64] is used here for computing the area fraction of a triangle submerged in $\tilde{\Omega}^-(t^{n+1})$. Any other second-order method can be applied. For example, a linear interpolation of signed distances along the edges of the triangle may be used equivalently, or a geometrical intersection between $\tilde{\Omega}^-(t^{n+1})$ and the triangle. The total submerged area of the face S_f is then the sum of the submerged areas of face-triangles

$$A_f^{n+1} := |\Omega^-(t^{n+1}) \cap S_f| = \sum_{k \in T_f} |\Omega^-(t^{n+1}) \cap T_k|, \tag{37}$$

where T_f is the set of indexes of the triangles in the triangulation of the face S_f. As mentioned above, any other two-phase flow simulation method that discretizes single-field Navier-Stokes equations but does not utilise phase-specific fluxes can be adapted to compute $|\Omega^-(t^{n+1}) \cap T_k|$.

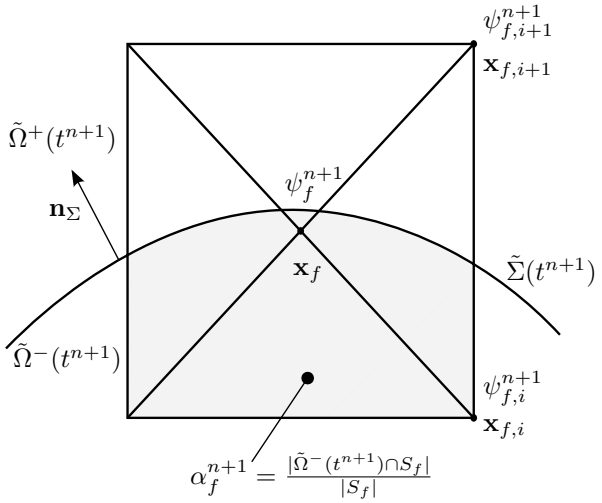

Figure 4: Computing area fractions from signed distances in the method.

The area fraction α_f^{n+1} is then computed as

$$\alpha_f^{n+1} := \frac{|\tilde{\Omega}^-(t^{n+1}) \cap S_f|}{|S_f|} = \frac{A_f}{|S_f|}, \tag{38}$$

as shown in fig. 4. Once the area fraction α_f^{n+1} is approximated, it is used to compute the face-centered densities required by eq. (33), namely

$$\rho_f^{n+1} = \alpha_f^{n+1} \rho^- + (1 - \alpha_f^{n+1}) \rho^+, \tag{39}$$

at the new time step, because the interface has been advected forward in time to t^{n+1} with the available velocity $\mathbf{v}^n$. The discretized continuity equation (eq. (24)) then attains the form

$$\rho_c^{o+1} = \rho_c^n + \frac{\Delta t}{|V_{\Omega_c}|} \sum_f \rho_f^{n+1} F_f^o, \quad F_f^o = \mathbf{v}_f^o \cdot \mathbf{S}_f. \tag{40}$$

It is important to note that, although ρ_f^{n+1} appears in eq. (40), ρLENT does not use an implicit discretization for eq. (40): ρ_f^{n+1} is geometrically computed from the fluid interface approximation $\tilde{\Sigma}^{n+1}$, so eq. (40) is solved exactly. The exact (iterative) evaluation of cell-center density at loop $o+1$, i.e. ρ_c^{o+1} from eq. (40), alongside eq. (29), further infers the possibility of exact numerical consistency for the discretized convective term in the single-field momentum equation, which is in fact achieved and supported by the results.

In addition to density, the viscosity is updated utilizing the area fraction α_f. Note that there is no need to calculate the cell-centered viscosity for the unstructured FVM discretization, only the face-centered viscosity is updated as follows

$$\mu_f^{n+1} = \alpha_f^{n+1}\rho^-\nu^- + (1-\alpha_f^{n+1})\rho^+\nu^+. \tag{41}$$

The non-linearity of the convective term in the momentum equation eq. (8), namely $\rho\mathbf{vv}$, is usually linearized when solving the single-field Navier-Stokes equations using the unstructured Finite Volume method. The convective term is discretized as

$$\int_{\Omega_c} \nabla\cdot(\rho\mathbf{vv})dV \approx \sum_{f\in F_c} \rho_f^{n+1} F_f^o \mathbf{v}_f^{n+1}. \tag{42}$$

Numerical consistency imposed by eq. (19) does not depend on the implicit or explicit discretization: the proportionality between the mass flux and the phase-specific flux, and the equivalence of the mass flux in the mass conservation equation and the momentum transport equation must both hold at any time, and in any iteration of the solution algorithm. Therefore, the requirement given by eqs. (29) and (30), is valid for an implicit discretization as well.

The volumetric flux F_f^o is initialized to F_f^n and iterated within the SAAMPLE [2] pressure-velocity coupling algorithm loop until $o = n+1$ is reached. The ρLENT algorithm is outlined in algorithm 1 and it extends the SAAMPLE algorithm [2]. It is relevant to note that F_f^o is iterated from F_f^n to F_f^{n+1} and p^o is solved for from p^n to p^{n+1} such that the discrete incompressibility condition $\sum_{f\in F_c} F_f^{n+1}$ is ensured.

Algorithm 1 The ρLENT solution algorithm.

while simulation time $\leq$ end time **do**
  Advect the interface to $\tilde{\Sigma}^{n+1}$. ▷ [1]
  Compute the signed-distance field ψ^{n+1} from $\tilde{\Sigma}^{n+1}$ at $\mathbf{x}_c, \mathbf{x}_f, \mathbf{x}_p$ in the narrow-band. ▷ [1]
  Compute α_c^{n+1} from $\psi_c^{n+1}, \psi_p^{n+1}$. ▷ [2]
  Compute the area fraction α_f^{n+1} from the signed distance fields $\psi_f^{n+1}, \psi_p^{n+1}$. ▷ Figure 4
  Compute the face-centered densities ρ_f^{n+1} using α_f^{n+1}. ▷ Equation (39)
  while F_f^o does not converge or $o < o_{max}$ **do**
    Solve the continuity equation using $\rho_f^{n+1}F_f^o$ for cell-centered densities ρ_c^{o+1}. ▷ Equation (40)
    while $r > \text{tol}_{ls}$ and $i < i_{max}$ **do**
      Use ρ_c^{o+1} and $\rho_f^{n+1}F_f^o$ in $p-\mathbf{v}$ coupling to compute $\mathbf{v}_c^{i+1}, F_f^{i+1}$. ▷ [2] and eq. (42)
    end while
  end while
    Make ρ_c^{n+1} consistent with $\tilde{\Sigma}^{n+1}$, i.e. $\rho_c^{n+1} = \alpha_c^{n+1}\rho^- + (1-\alpha_c^{n+1})\rho^+$.
    Make μ_c^{n+1} consistent with $\tilde{\Sigma}^{n+1}$, i.e. $\mu_c^{n+1} := \alpha_c^{n+1}\rho^-\nu^- + (1-\alpha_c^{n+1})\rho^+\nu^+$.
end while

The $p-\mathbf{v}$ coupling - mentioned in the step 8 in algorithm 1 - requires some further explanation. The semi-implicit discretization (with the convective term linearized as an explicit mass-flux and implicit velocity) of the single-field momentum equation using the implicit collocated unstructured finite volume method [55, 56], results in

$$a_c \mathbf{v}_c^{n+1} + \sum_{k \in N_c} a_k \mathbf{v}_k^{n+1} = -(\nabla p)_c^{n+1} - [(\nabla \rho)^{n+1} \cdot (\mathbf{g} \cdot \mathbf{x})]_c + (\mathbf{f}_\Sigma)_c^{n+1}, \tag{43}$$

where N_c is the index-set of cells that are face-adjacent to cell Ω_c, and the total pressure is expressed using the dynamic and the hydrostatic pressure. The diagonal coefficient a_c corresponds to the cell Ω_c, and k denotes the coefficients contributed from cells that are face-adjacent to Ω_c. We discretize the surface tension force $(\mathbf{f}_\Sigma)_c^{n+1})$ using the semi-implicit model from [2].

Equation eq. (43) is also discretized semi-implicitly, because of the linearized convective term, that contributes the volumetric flux F_f to the $a_{c,k}$ coefficients in eq. (43). Linearizing the convective term introduces a need for iteration. Iterations are also introduced by splitting eq. (43) into two equations: one for $\mathbf{v}_c^{n+1}$, and another for $\mathbf{p}_c^{n+1}$. Dividing the equation eq. (43) with a_c and applying the discrete divergence $\nabla_c \cdot$, results in the pressure equation

$$\begin{aligned} \sum_{f \in F_c} \left(\frac{1}{a_c}\right)^o (\nabla p)_f^{i+1} \cdot \mathbf{S}_f = \sum_{f \in F_c} \left(\frac{1}{a_c}\right)^o [\mathbf{H}(\mathbf{v}^i)]_f \cdot \mathbf{S}_f + \sum_{f \in F_c} \left(\frac{1}{a_c}\right)^o [(\nabla \rho)^i \cdot (\mathbf{g} \cdot \mathbf{x})]_f \cdot \mathbf{S}_f + \\ \sum_{f \in F_c} \left(\frac{1}{a_c}\right)^o \sigma \kappa_f^{n+1} (\nabla \alpha)_f^i \cdot \mathbf{S}_f, \end{aligned} \tag{44}$$

where we use the CSF model [43] to model the surface tension force $(\mathbf{f}_\Sigma)_f \approx \sigma \kappa_f (\nabla \alpha)_f$. The discrete divergence-free condition imposed on $\mathbf{v}_c^{n+1}$ in eq. (43) results in the divergence-free volumetric flux

$$\sum_{f \in F_c} F_f^o = 0, \tag{45}$$

used as the control variable for the convergence of outer iterations o by the SAAMPLE algorithm [2]. The outer iterations o are used for linearizing the volumetric flux as described above and contribute the volumetric flux to the coefficients $a_{c,k}$, from eq. (43), while $\mathbf{H}(\mathbf{v})$ in eq. (44) is the contribution of convection and diffusion operators from face-adjacent cells in eq. (43). Note that $(\nabla \rho)_{c,f}^{n+1}$ and the implicit part of $(\mathbf{f}_\sigma^{n+1})_{f,c}$ are known at t^{n+1} from $\mathbf{f}_\sigma^{n+1} := \mathbf{f}_\sigma^{n+1}(\{\mathbf{x}_p^{n+1}\}_{p \in P})$, and eq. (40).

This segregated solution for $(p_c^{n+1}, \mathbf{v}_c^{n+1})$ is standard in the context of collocated unstructured finite volume method [56]: the inner iterations and the assembly of the pressure equation originates from the PISO algorithm [65], the outer iterations originate from the SIMPLE algorithm [66], and the tolerance-based control of outer iterations is described in detail in [2]. In addition, the implementations of the LENT method [1], the SAAMPLE algorithm [2] and the ρLENT method are publicly available [9]. This description, the details on the tolerance-based outer iteration control in [2], and the publicly available implementation in OpenFOAM, provide sufficient information for an interested reader willing to understand or further extend the methodology.

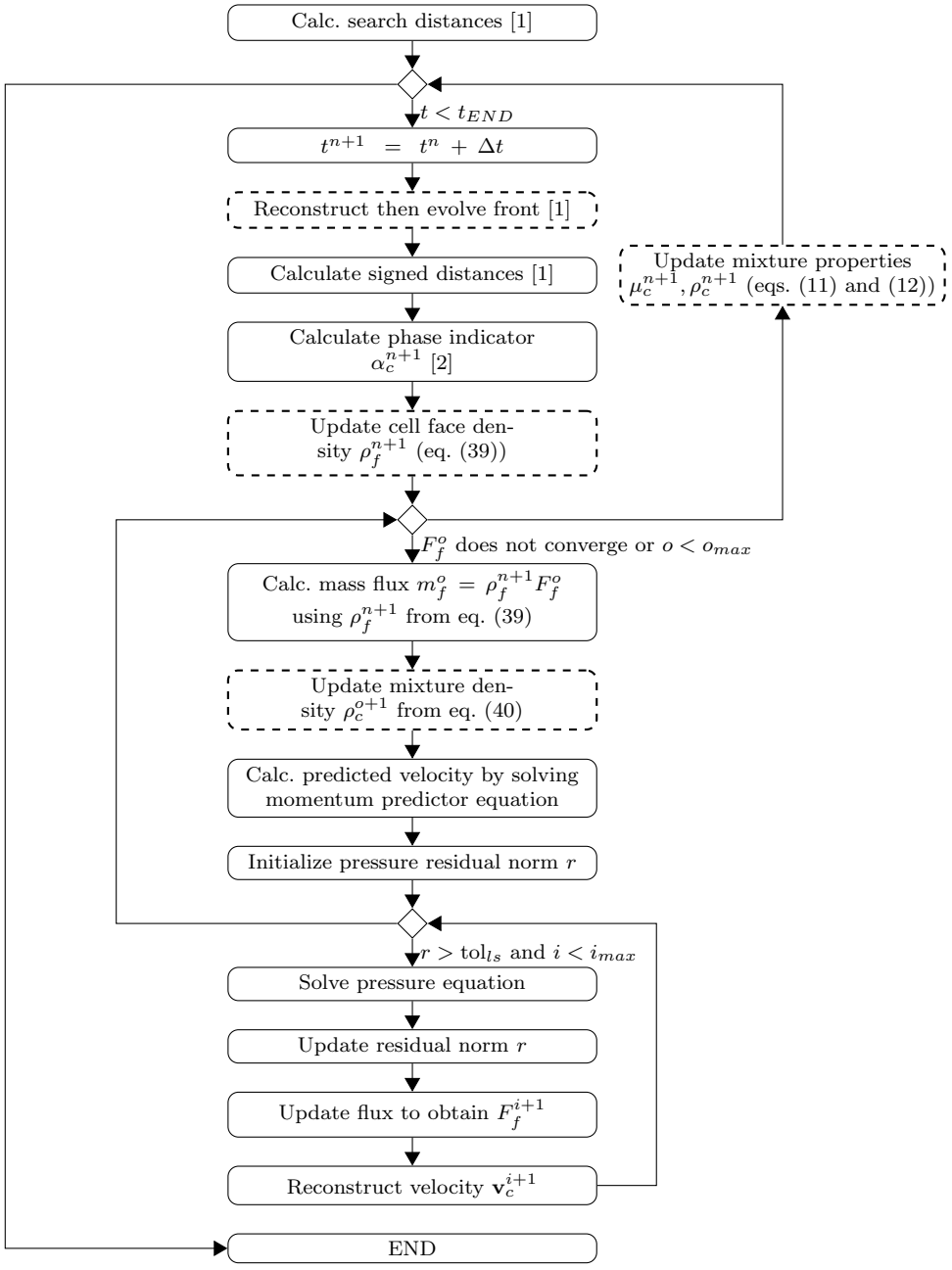

Figure 5: Flowchart of the ρLENT method. The dashed blocks denote the new and modified elements of the SAAMPLE method [2]. The indices o_{max} and i_{max} in the flowchart indicate the maximal iteration numbers for the outer and inner loop, respectively, while tol_{ls} denotes the prescribed linear solver tolerance.

3.4. Volume correction method

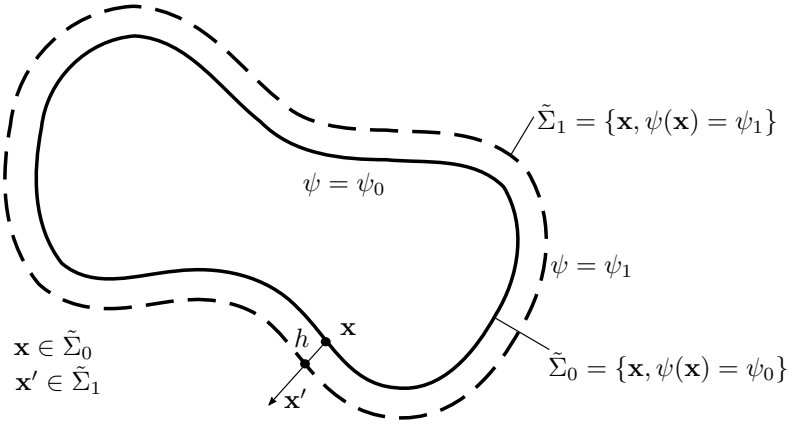

Figure 6: The volume correction method: iso-value compensates the volume-change.

Level Set / Front Tracking methods are Lagrangian / Eulerian methods that kinematically evolve the fluid interface without utilising fluxes through control-volume boundaries and are therefore inherently not mass(volume)-conservative. Rising bubble and oscillating droplet simulations are presented in the results section to demonstrate the benefits of the ρLENT method for stronger momentum interaction between fluid phases that have strongly different densities. Mass conservation is crucial for accurately simulating rising bubbles (Singh and Shyy [67], Hua and Lou [68], Hua et al. [69], Pivello et al. [70]). In particular, Hua and Lou [68] conducted comparative analyses which revealed that mass conservation carries equivalent importance to mesh resolution and domain size in influencing the accuracy. The Front reconstruction in the LENT method [1, 2] uses marching tetrahedrons with linear interpolation of the iso-surface root-points Treece et al. [63], that causes volume loss. To demonstrate the benefits of the proposed ρLENT method for handling high density ratios with stronger interface deformation and momentum exchange, we ensure volume conservation using by extending/contracting the Front with a modified iso-value.

Figure fig. 6 depicts the volume correction at time step n, where $\tilde{\Sigma}_0$ denotes the Front at the time step n. The value $\psi_0 = 0$ is the iso-value used to reconstruct the $\tilde{\Sigma}_0$ at t^n. From $\tilde{\Sigma}_0$ that contains volume-conservation errors, we compute the corrected Front $\tilde{\Sigma}_1$, as $\tilde{\Sigma}_0$ extended in the normal direction by h. We consider volume loss, with no loss of generality in the case of volume gain. For sufficiently small h, for any $\mathbf{x} \in \tilde{\Sigma}_0$, we define $\mathbf{x}' := \mathbf{x} + h\mathbf{n}_\Sigma(\mathbf{x}), \mathbf{x}' \in \tilde{\Sigma}_1$. The linear Taylor-series approximation

$$\psi(\mathbf{x}') \doteq \psi(\mathbf{x}) + \nabla\psi(\mathbf{x}) \cdot h\mathbf{n}_\Sigma(\mathbf{x}), \tag{46}$$

with $\psi(\mathbf{x}) = 0$ by the definition of an iso-surface $\forall \mathbf{x} \in \tilde{\Sigma}_0$, results in

$$\psi(\mathbf{x}') \doteq h\nabla\psi(\mathbf{x}) \cdot \mathbf{n}_\Sigma(\mathbf{x}). \tag{47}$$

Since Level Set / Front Tracking ensures $\nabla\psi(\mathbf{x}) = \mathbf{n}_\Sigma$ and thus $\nabla\psi(\mathbf{x}) \cdot \mathbf{n}_\Sigma(\mathbf{x}) = 1$ by geometrically re-distancing ψ from the reconstructed Front $\tilde{\Sigma}_0^n$,

$$\psi(\mathbf{x}') = h. \tag{48}$$

The height h is expressed from the change in volume between $\tilde{\Sigma}_0$ and $\tilde{\Sigma}_1$

$$\begin{aligned} \int_{\tilde{\Sigma}_0} h\, dS &= V_{target} - V_{ini}, \\ h &= \frac{V_{target} - V_{ini}}{\int_{\tilde{\Sigma}_0} 1\, dS}, \end{aligned} \tag{49}$$

Volume V_{target} is the target volume and known before the reconstruction, and we aim to recover V_{target}'s corresponding front $\tilde{\Sigma}_1$. The volume V_{ini} is computed from the initially reconstructed $\tilde{\Sigma}_0$. If volume loss really occurred, then $V_{target} > V_{ini}$, and $h > 0$, so we extend $\tilde{\Sigma}_0$ in the direction of $\mathbf{n}_\Sigma$ by reconstrucing an iso-surface $\tilde{\Sigma}_1 = \{\mathbf{x}' : \psi(\mathbf{x}') = h\}$. However, if volume gain occured, $V_{target} < V_{ini}$, so $h < 0$, and reconstrucing an iso-surface $\tilde{\Sigma}_1 = \{\mathbf{x}' : \psi(\mathbf{x}') = h\}$ shrinks $\tilde{\Sigma}_0$ in the normal direction.

The volume V_{ini} is computed geometrically [44] as

$$V_{ini} = \frac{1}{3} \left| \sum_{e=1}^{N_{\tilde{\Sigma}_0}} \mathbf{x}_e \cdot \mathbf{S}_e \right|, \tag{50}$$

where $N_{\tilde{\Sigma}_0}$ is the number of triangles in $\tilde{\Sigma}_0$, $\mathbf{x}_e$ is a centroid, and $\mathbf{S}_e$ the area-normal vector of the e-th triangle in $\tilde{\Sigma}_0$. At reconstruction time step t^n, the front is first reconstructed using the iso-value $\psi_0 = 0$, as shown in fig. 6. The volume $V^n(\psi_0 = 0)$ is then calculated w.r.t eq. (50). Since the loss/gain of volume between successive reconstructions is small ($\mathcal{O}(10^{-4})$), the compensated extension/contraction is uniformly distributed across the Front. The iso-value adjustment given by eq. (49) is then discretized as

$$h = \frac{V(\tilde{\Sigma}_1) - V_{ini}}{\sum_{e=1}^{N_{\tilde{\Sigma}_0}} |\mathbf{S}_e|}, \tag{51}$$

in which $|\mathbf{S}_e|$ denotes the area of the e-th triangle. Reconstruction with the new iso-value $\psi_1 = h^n$ generates a volume-conserved Front, as illustrated by the solid line on the right in fig. 6.

4. Verification and validation

The hybrid Level Set / Front Tracking method is not strictly volume conservative, and volume errors arise from three sources. First, the iso-surface reconstruction - that handles the topological changes of the fluid interface - introduces volume errors by interpolating the level-set function. This error source can be reduced using higher-order level set function interpolation. Second, the Front Tracking method approximates the fluid interface as a surface triangulation and advects the interface in a co-moving reference frame by displacing the triangulation points along Lagrangian trajectories. The volume errors introduced by Front Tracking are reducible significantly by a second (or higher)-order temporal integration of the Lagrangian displacements. The third source of volume conservation errors is the phase-indicator model: we approximate volume fractions from signed distances stored at cell centers and cell-corner points [2]; however, we are investigating a more accurate geometrical intersection between the Front and the volume mesh [44]. The volume conservation of the hybrid Level Set / Front Tracking method depends on the physics of the problem. For the verification problems, the ρLENT method recovers very low maximal relative volume conservation

errors of $5.13 \cdot 10^{-4}$ for the coarsest resolution of only 6 cells per droplet diameter and $5.49 \cdot 10^{-5}$ for the finest resolution of 26 cells per droplet diameter. The volume conservation errors of such small magnitude have no effect on the numerical stability of the two-phase momentum convection term, so their detailed visualization is omitted for brevity.

Secondary data presented in this section in the form of diagrams and tables [71], the snapshot of the LENT implementation used in this manuscript [72], and the active development repository of the LENT method as an OpenFOAM module [73] are publicly available.

4.1. Time step size

The time step size limit due to the CFL condition is given by

$$\Delta t \leq \Delta t_{CFL} = \frac{h}{U}, \tag{52}$$

where h is cell length and U is a characteristic velocity. In the cases, h is the minimum cell size, while U is equal to magnitude of the ambient flow velocity vector, i.e. $U = |\mathbf{v}_a| = 1$. Another restriction for the time step size arises from the propagation of capillary waves on interfaces between two fluids. This time step constraint is firstly introduced by Brackbill et al. [43], and afterwards revised by Denner and van Wachem [74]. It has the form

$$\Delta t \leq \Delta t_{cw} = \sqrt{\frac{(\rho_d + \rho_a)h^3}{2\pi\sigma}}, \tag{53}$$

in which ρ_d and ρ_a are density of droplet and ambient fluid, respectively, σ is the surface tension coefficient. In the case setup procedure, the method devised by Tolle et al. [2] is followed, i.e., using a compare function

$$\Delta t = \min\left(k_{cw}\Delta t_{cw},\ k_{CFL}\Delta t_{CFL}\right) \tag{54}$$

where k_{cw} and k_{CFL} are arbitrary scale factors between 0 and 1. In the following, $k_{cw} = 0.5$ and $k_{CFL} = 0.2$ are used.

4.2. Translating droplet

Following the setup of Popinet [75], a sphere of radius $R = 0.2$ translates in a rectangular domain having side lengths $L_x = L_y = 5R, L_z = 6R$. The initial position of the sphere's centroid is $C_x = C_y = 0.5, C_z = 0.4$. One corner of the rectangular domain locates in the origin as shown in fig. 7. The boundary conditions of the rectangular domain are set as follows: $\nabla\mathbf{v} = 0$ and $p = 0$ for the outlet, $\mathbf{v} = \mathbf{v}_a$ and zero gradient $\nabla p = 0$ for the pressure at the mantle and the inlet. The initial conditions for internal field is set to $p(t_0) = 0$ and $\mathbf{v}(t_0) = \mathbf{v}_a$. The end time of simulation is set to $t_{end} = 0.41$ s, which corresponds to a droplet displacement of one diameter.

Two groups of cases are tested to verify the ρLENT method, their parameters are listed in table 1. For the first group, only the advection of momentum and pressure term are considered, and the ambient flow has a constant density $\rho_a = 1$, while the density of the droplet ρ_d varies between $(1, 10^2, 10^3, 10^4)$, resulting in four density ratios. Three mesh resolutions $N \in (16, 32, 64)$ are tested. For each mesh resolution N, the domain is discretized equidistantly into $1.2N^3$ hexahedral cells, as shown in fig. 8. The exact solution is given by $\mathbf{v}_c^{n+1} = \mathbf{v}_c^n = \mathbf{v}_c(t_0) = \mathbf{v}_a$ and can be used to verify the numerically consistent discretization of the single-field conservative two-phase momentum convection.

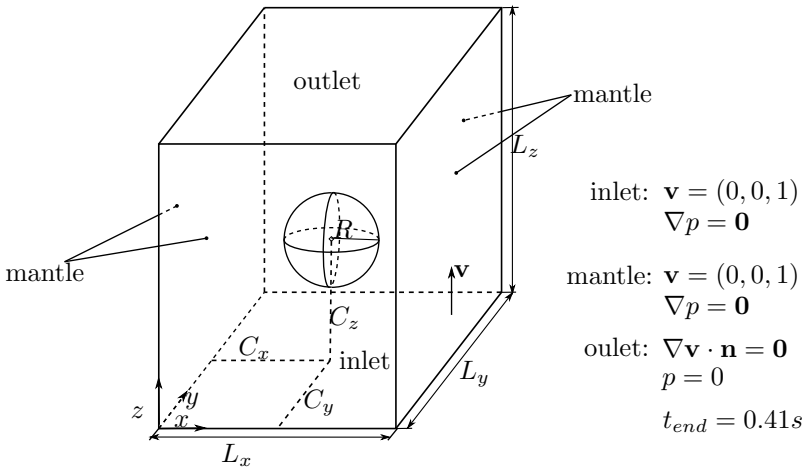

$$R = 0.2, C_x = C_y = 0.5, C_z = 0.4, L_x = L_y = 5R, L_z = 6R$$

Figure 7: Translating droplet case setup.

		Parameters range			
	Momentum equation	Density ratio	Resolution	Kinematic viscosity	Surface tension coefficient
Group 1	$\partial_t(\rho\mathbf{v}) + \nabla \cdot (\rho\mathbf{v} \otimes \mathbf{v}) = -\nabla p$	$(1, 10^2, 10^3, 10^4)$	$(16, 32, 64)$	0	0
Group 2	$\partial_t(\rho\mathbf{v}) + \nabla \cdot (\rho\mathbf{v} \otimes \mathbf{v}) = -\nabla p - (\mathbf{g} \cdot \mathbf{x})\nabla\rho + \nabla \cdot \mu \left(\nabla\mathbf{v} + (\nabla\mathbf{v})^T\right) + \mathbf{f}_\Sigma$	$(1, 10^2, 10^3, 10^4)$	$(16, 32, 64)$	$(0.057735, 0.018257, 0.0057735, 0.0)$	1

Table 1: The parameters range of the case group 1 and the case group 2.

Viscosity and surface tension forces are included in the second test case group. The same range of density ratios is simulated, $\rho^-/\rho^+ \in (1, 10^2, 10^3, 10^4)$. The same kinematic viscosity is used for the ambient and the droplet phase, namely $\nu \in (0.057735, 0.018257, 0.0057735, 0.0)$.

The surface tension coefficient is constant $\sigma = 1$.

4.2.1. Droplet translation without viscosity and surface tension forces

When the momentum is transported only by advection, no forces are exerted on the droplet body and surface. As a result, the velocity field in the overall domain should remain spatially constant and equal to $\mathbf{v}_a = (0, 0, 1)$. The maximum norm L_∞ is employed to measure how much the numerical velocity deviates from the analytical one, i.e.,

$$L_\infty(\mathbf{v}) = \max_i \left(\frac{\|\mathbf{v}_i - \mathbf{v}_a\|}{\|\mathbf{v}_a\|} \right), \tag{55}$$

where $\mathbf{v}_i$ denotes velocity of all cells. The previous SAAMPLE method [2] can cause large non-physical interface deformations leading to a complete deterioration of the solution, visible for a verification configuration in the left image in fig. 10. The deterioration is amplified by the $p - \mathbf{v}$ coupling algorithm that will calculate a pressure field p that enforces $\nabla \cdot \mathbf{v} = 0$. This, in turn, causes artificial acceleration in all cells where $\mathbf{v}_c^{n+1} \neq \mathbf{v}_a$. The consistent ρLENT method ensures the shape of the droplet is preserved, as shown on the right image in fig. 10.

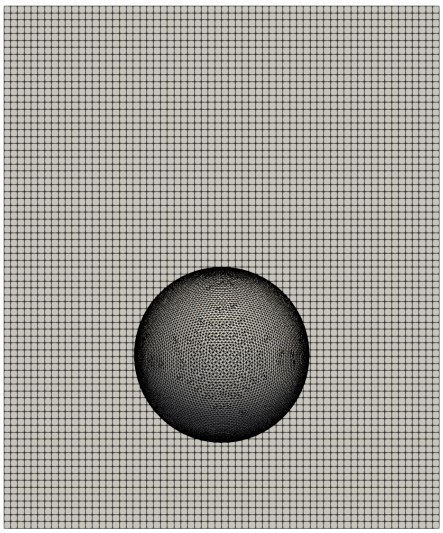

Figure 8: Half section of mesh $N = 64$, droplet at initial position.

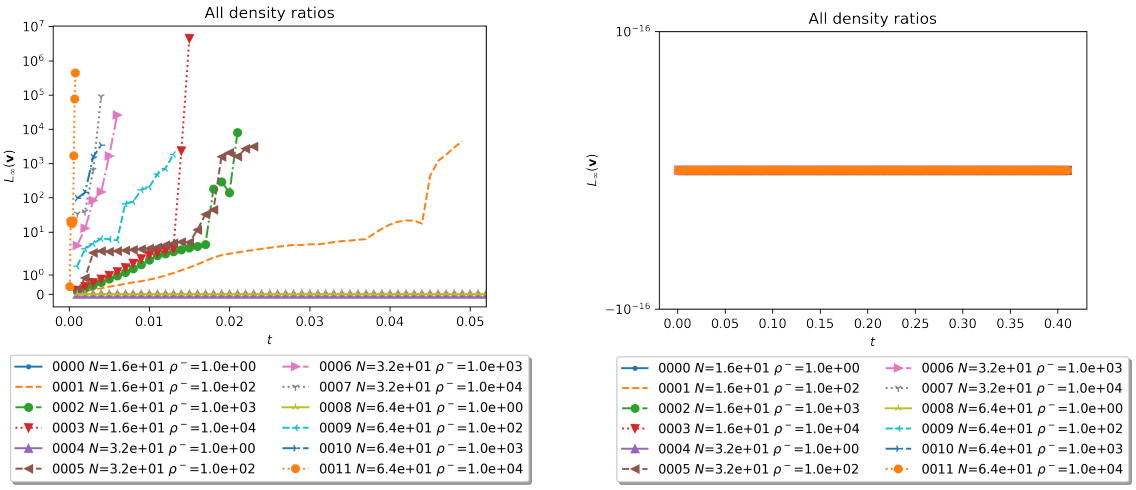

(a) SAAMPLE method.

(b) ρLENT method.

Figure 9: Temporal evolution of velocity error norm $L_\infty(\mathbf{v})$: the left figure depicts the results from SAAMPLE algorithm, the right shows the results from ρLENT method.

The fig. 9a contains the velocity error calculated with the old, inconsistent method. Every line in the diagram is labeled by the number of the case, mesh resolution N, and droplet density ρ^-. The default ambient density is 1. Thus, the ρ^- also represents the density ratio. As shown in fig. 9a, all cases with a density ratio higher than 1, namely $\rho^- > 1$, diverge and stop at early stage. Cases with a very high density ratio of 10^4 (e.g., case 0011 and 0003) fail catastrophically. The complete

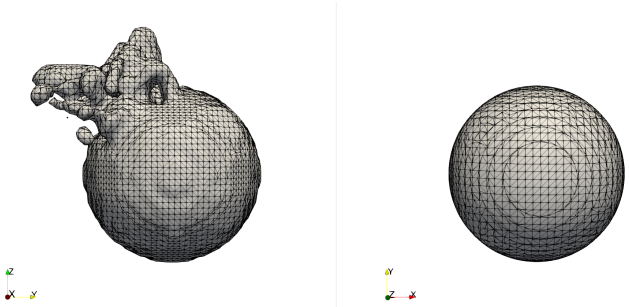

Figure 10: Comparison of the strong interface deformation with SAAMPLE method (left) and the numerically consistent interface shape of the ρLENT method. Parameters: $N = 64$, $\rho^-/\rho^+ = 10^4$, $t = 0.0008s$.

results are shown in fig. A.20, in Appendix A.

When ρLENT is used, as shown in fig. 9b, the velocity error remains exactly 0 in all cases. This means that the interface velocity remains consistent with the ambient flow and is unaffected by the mesh resolution and density ratio. The results demonstrate the exact recovery of numerical consistency for the advection of the two-phase momentum, using an implicitly discretized momentum term in a conservative formulation of single-field two-phase Navier-Stokes equations.

4.2.2. Droplet translation with viscosity and surface tension forces

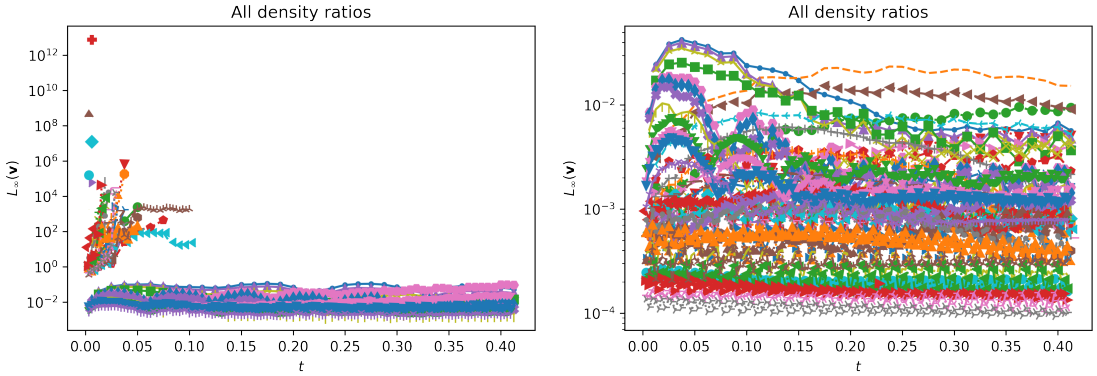

(a) SAAMPLE: interface stable only for cases with density ratio $\rho^-/\rho^+ = 1$

(b) ρLENT: interface stable for density ratios $\rho^-/\rho^+ \in (1, 10^2, 10^3, 10^4)$

Figure 11: Temporal evolution of velocity error norm $L_\infty(\mathbf{v})$ for the viscous flow with surface tension forces: the left diagram depicts the results from the SAAMPLE method, and the right diagram contains the results from the ρLENT method. The legends of these diagrams are large, and the full information is available in Appendix A: fig. A.18 for fig. 11a, fig. A.19 for fig. 11b.

Here, viscous and capillary forces are taken into account when solving the momentum equation. Since SAAMPLE is a well-balanced algorithm [2] - SAAMPLE balances the discrete surface tension force exactly with the pressure gradient when constant curvature is used, using the same discretization for the pressure gradient and the surface-normal gradient of the volume fraction [75]. The

force-balance is maintained also if the curvature is exactly calculated and propagated as a constant in the interface-normal direction. For numerically approximated curvature, the balance is obtained on a dissipation timescale with respect to initial perturbations. The translating droplet test case combines the force-balance requirement in the droplet's frame of reference, with the requirement for numerical consistency of the two-phase momentum advection. In the absence of gravity, such a droplet does not accelerate or decelerate. The temporal evolution of L_∞ is shown in fig. 11. The inconsistent method remains stable only for $\rho^-/\rho^+ = 1$. For the results of all other cases, i.e., with $\rho^-/\rho^+ > 1$, the velocity error increases exponentially, and the simulations crash. In contrast, as depicted in fig. 11b, the ρLENT demonstrates numerically stable results for all tested density ratios. Additional numerical errors are introduced compared with two-phase momentum advection, specifically when approximating the curvature [2]. The approximation of curvature in [2] recovers accurate L_2 norms of the curvature errors for a sphere, in the range $[10^{-4}, 10^{-3|}]$ for discretization lengths in the range $[128^{-1}, 16^{-1}]$ in the unit-box solution domain. Because of the numerically approximated curvature, L_∞ cannot exactly be equal to zero, as shown in fig. 9b. However, as seen in fig. 11b, the final L_∞ error given by eq. (55) 10^{-4} and 10^{-2}, which is acceptable.

4.2.3. Translating sub-millimeter droplet with realistic physical properties

materials/properties (25 °C)	density ($\mathrm{kg\,m^{-3}}$)	kinematic viscosity ($\mathrm{m^2\,s^{-1}}$)	surface tension ($\mathrm{N\,m^{-1}}$)	density ratio
air	1.1839	1.562×10^{-5}	− − −	− − − [76]
water	997.05	8.926×10^{-7}	0.07213 (in air)	842.17 (in air) [76]
mercury	13.5336×10^3	1.133×10^{-7}	0.4855 (in air)	11431.37(in air) [76]
silicone oil (cSt 10)	0.934×10^3	1.088×10^{-5}	0.0201 (in air)	788.92(in air) [77]
silicone oil (cSt 50)	0.96×10^3	5×10^{-5}	0.032 (in water)	0.96 (in water) [78]

Table 2: Realistic fluid properties are combined into four tests: water droplet/air ambient, mercury droplet/air ambient, silicone oil droplet/air ambient, silicone oil droplet/water ambient.

The physical properties including densities, viscosities, and surface tension coefficients in the widely used translated droplet case from Popinet [75] are not related to physical two-phase flows systems. We have adapted the case and used small droplet dimensions to challenge the method in terms of surface tension force approximation for capillary problems, and used real-world fluid pairings with challenging density ratios.

Table 2 contains the physical properties used for the test-case configuration of the translating sub-millimeter droplet with realistic physical properties. In terms of size, a spherical droplet of radius $R = 0.25\,\mathrm{mm}$ is translating a distance of three diameters with velocity $0.01\,\mathrm{m/s}$ in z-direction of the rectangular solution domain ($L_x = L_y = 5R, L_z = 10R$). The initial centroid position of the droplet is $(2.5R, 2.5R, 2R)$. Surface tension and viscous forces are not considered for this setup.

As depicted in fig. 12, it is obvious that $L_\infty(\mathbf{v})$ remains stable over time when the droplet translates. Even in the cases with a density ratio of over 10^4, as shown in fig. 12d, no matter how high the resolution is, the results from ρLENT the method can reach machine precision.

The fig. 13 illustrates the results of the same realistic droplets' cases, considering the influence of viscous forces and surface tension. It is observed that the errors decrease as the resolution increases, reaching magnitudes as low as 10^{-5} for all cases. This indicates the excellent capability of ρLENT to handle a wide range of density ratios in such cases.

Apart from the observation mentioned above, table 3 reveals another advantage of ρLENT method - high computational efficiency. As shown in table 3, the ρLENT method demonstrates very high computational efficiency in serial. Increasing the parallel computational efficiency requires

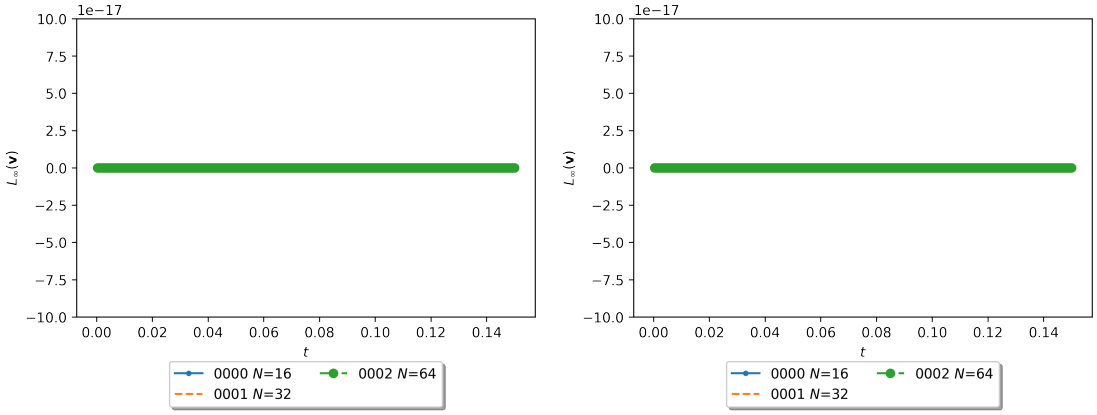

(a) Silicone oil droplet in water, density ratio 0.96

(b) Silicone oil droplet in air, density ratio 788.92

(c) Water droplet in air, density ratio 842.17

(d) Mercury droplet in air, density ratio 11431.37

Figure 12: Temporal evolution of velocity error norm $L_\infty(\mathbf{v})$ with pure advection: ρLENT method used in simulating two-phase flows with different density ratios, mesh resolution: $N \in (16,\ 32,\ 64)$.

further research, specifically, regarding a more efficient message-passing parallel implementation for unstructured Level Set / Front Tracking.

4.2.4. Oscillating droplet

An ellipsoidal droplet is submerged in an ambient fluid with an approximate axially symmetric solution provided by Lamb [79]. The solution can be represented as a summation of a constant and a Legendre polynomial $P_n(\cos\theta)$, i.e.,

$$R(\theta, t) \doteq R_0 + a_n P_n(\cos\theta)\sin(\omega_n t), \quad \theta \in [0, 2\pi], \tag{56}$$

where R_0 is the initial unperturbed radius, a_n is the amplitude of the n-th oscillation mode, θ is the angle between the radius line of a droplet point and the symmetric axis, ω_n represents the

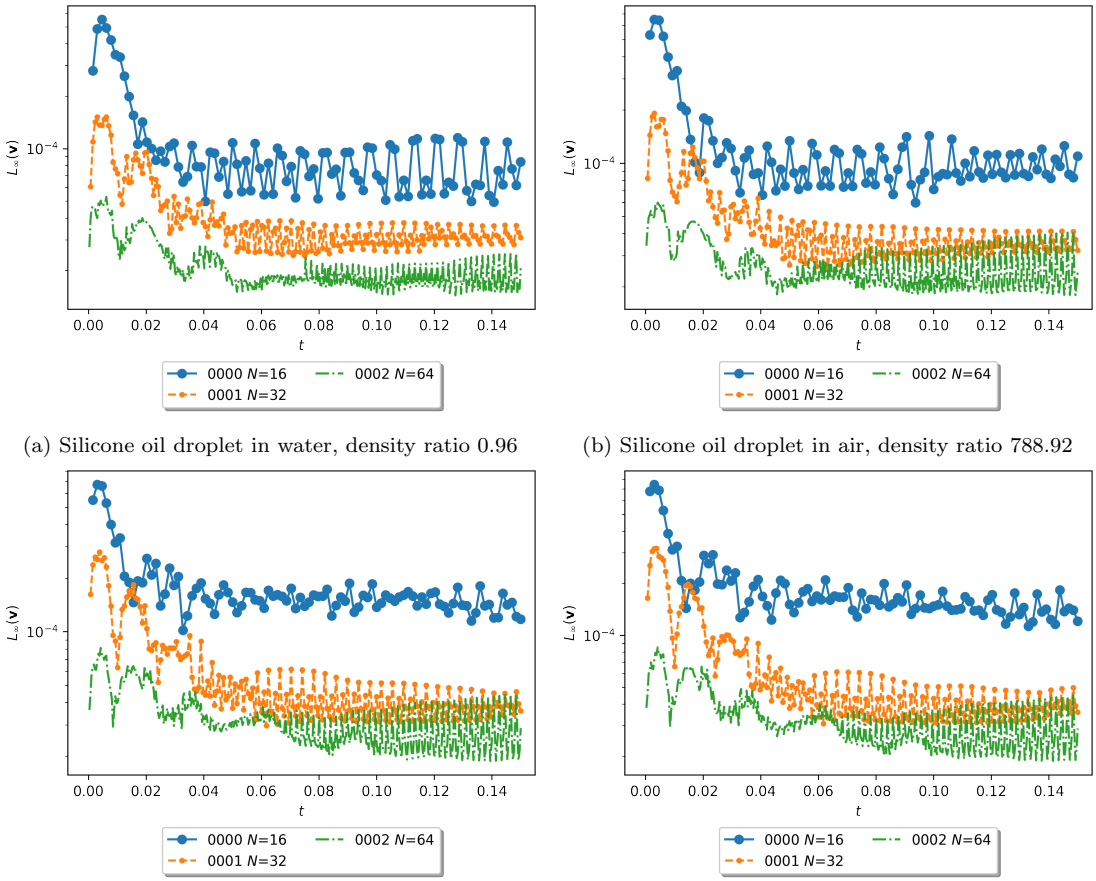

(a) Silicone oil droplet in water, density ratio 0.96

(b) Silicone oil droplet in air, density ratio 788.92

(c) Water droplet in air, density ratio 842.17

(d) Mercury droplet in air, density ratio 11431.37

Figure 13: Temporal evolution of velocity error norm $L_\infty(\mathbf{v})$ with the effect of viscosity and surface tension: ρLENT method used in simulating two-phase flows with different density ratios, mesh resolution: $N = 16, 32, 64$.

oscillation frequency. The latter ω_n has the form

$$\omega_n^2 = \frac{n(n+1)(n-1)(n+2)\sigma}{[(n+1)\rho_d + n\rho_a]R_0^3}, \tag{57}$$

where n is the mode number, ρ_d, ρ_a represent the droplet and ambient flow density respectively, σ indicates the surface tension coefficient. Lamb [79] derived eq. (56) neglecting the viscous effect, and used constant a_n. Chandrasekhar [80], Miller and Scriven [81], Prosperetti [82] extended the expression of a_n to include the influence of the viscosity, where the amplitude a_n decays exponentially over time by

$$a_n(t) = a_0 e^{-\gamma t}, \ \gamma = \frac{(n-1)(2n+1)\nu}{R_0^2}, \tag{58}$$

where ν is the kinematic viscosity. Hiller and Kowalewski [83] conducted a series of experiments to validate the decay expression.

cases	resolution	serial execution time (s)
silicone oil droplet / water	16	6.62
	32	74.34
	64	929.79
water droplet / air	16	7.77
	32	91.64
	64	1324.38
mercury droplet / air	16	7.71
	32	94.57
	64	1334.36
silicone oil droplet / air	16	7.31
	32	83.43
	64	1318.43

Table 3: Serial execution time for the ρLENT method.

We have applied the physical properties of mercury and air from 2 to the droplet and the ambient fluid. The droplet interface is initialized with the parameters: $R_0 = 0.01$, $n = 2$, $\epsilon = 0.00025$, $t = \pi/(2\omega_n)$ and the center $(0.0200001, 0.0199999, 0.020000341)$. The computational domain size is $(0, 0, 0) \times (0.04, 0.04, 0.04)$. The gravity is neglected in this case. At the simulation's beginning, the droplet and the flow are still, i.e. $\mathbf{v}(t = 0) = 0$ holds for the whole field. Since the analytical frequency ω_a can be acquired from eq. (57), the results are evaluated by an error norm

$$L_1(\omega) = \frac{|\omega - \omega_a|}{\omega_a}. \tag{59}$$

Three mesh resolutions are tested to verify the convergence of both methods. The results of the SAAMPLE[2] and ρLENT with increasing mesh resolutions are summarized in the table 4. As shown in fig. 14, the oscillating frequencies calculated from SAAMPLE do not converge. On the contrary, when deploying the new consistent method, L_1 norm exhibits second-order convergence.

Grid size h	Background mesh		Front mesh		SAAMPLE		ρLENT	
	Points	Cells	Points	Tris.	Frequency	L_1 norm	Frequency	L_1 norm
0.0016	17576	15625	3150	6296	16.255923	0.040397	16.346002	0.035080
0.0008	132651	125000	12662	25320	16.444685	0.029254	16.888921	0.003031
0.0004	1030301	1000000	50732	101460	16.218606	0.042600	16.928274	0.000708

Table 4: The analysis of the oscillation frequency convergence and its comparison between the SAAMPLE method and the consistent ρLENT method.

4.3. Rising bubble

In this test case, we apply the proposed method to a single bubble rising in quiescent viscous liquid. We test the configuration from Anjos et al. [84], who simplified the rising bubble experiments previously conducted by Bhaga and Weber [85] and selected three different viscosity ratios to perform tests and comparisons. In this section, we focus on the most challenging case, i.e. the case with the smallest viscosity ratio, which corresponds Morton number $Mo = g\nu_l^4/\rho_l\sigma^3 = 1.31$, where g is the gravitational acceleration value, and ν_l, ρ_l, σ indicate the viscosity, density of the ambient liquid and the surface tension. The initial state of the air bubble is idealized to be spherical with

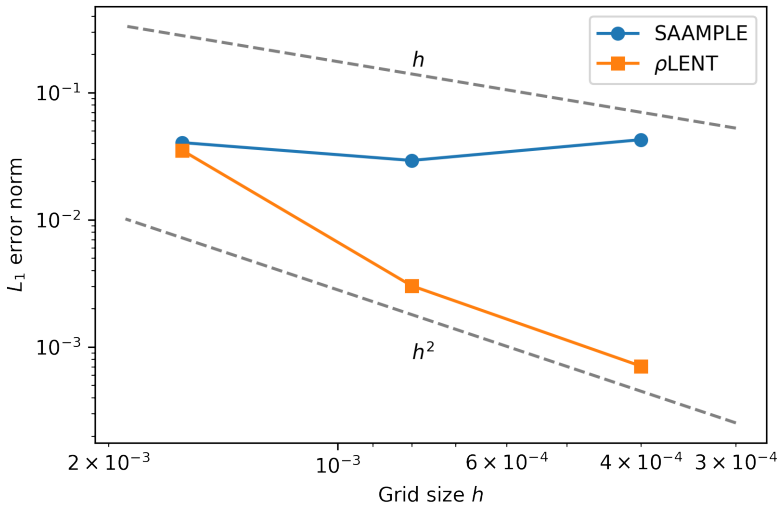

Figure 14: L_1 norms of the oscillation frequency errors.

a diameter of $D = 2.61$ cm. The physical properties of the air are characterized by a viscosity of 1.78×10^{-5} kg/ms and a density of 1.225 kg/m^3, whereas the properties of the liquid are defined by a viscosity of 0.54 kg/ms and a density of 1350 kg/m^3. Additionally, the surface tension between the air bubble and the liquid is 0.078 N/m. The computational domain is defined as $(-4D, -4D, -2D) \times (4D, 4D, 6D)$, which show the positions of space diagonal vertices of the computational domain, and the initial position of the bubble is set as the origin, $(0, 0, 0)$.

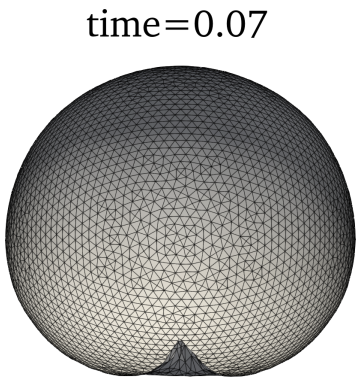

Figure 15: SAAMPLE method: the collapsed bubble shape caused by numerical inconsistency.

As the parallel computing module in the ρLENT method is still in the developmental phase, the entire domain was resolved using a single core. Consequently, relatively coarse meshes were utilized to simulate the motion of the bubble, i.e. $N \in (64,\ 96,\ 128,\ 160)$, where N indicates the

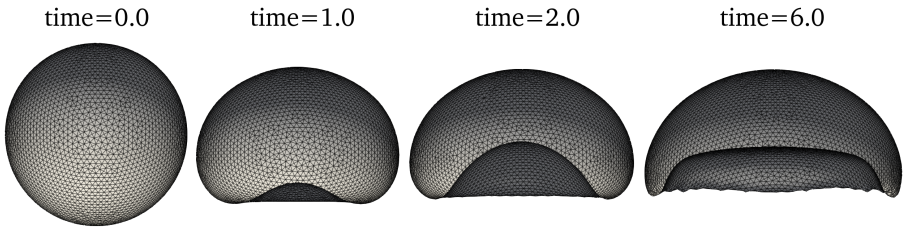

Figure 16: ρLENT: the temporal evolution of bubble's shape with resolution $N = 128$.

grid numbers in all three directions of the computational domain. To estimate the results, a set of dimensionless characteristic variables was introduced as follows:

$$\mathbf{w} = \frac{\mathbf{v}}{\sqrt{gD}},\ t = \sqrt{\frac{g}{D}}\tau, \tag{60}$$

where τ indicates the realistic time. When deploying the inconsistent method, the simulation crashed at an early stage, as shown in 15. Inconsistent method deployment resulted in a simulation crash at an early stage. The velocity of the bubble's bottom region increased abruptly, causing the front's vertices in that region to have much higher velocity than the neighbor region, which explains the bottom sharp cone formation as shown in Figure 15. Conversely, Figure 16 depicts the temporal evolution of the bubble's shape using the consistent method with $N = 128$. The predicted bubble shapes show good agreement with the previous simulation results [68, 69, 84] and the experimental results [85]. Additionally, 17 shows a comparison of the bubble's rising velocities between our ρLENT method and some previous works. At the acceleration stage, the predicted rising velocity from ρLENT method with the finest mesh $N = 160$ agrees remarkably well with the results from Anjos et al. [84], whereas the velocities from the cases with coarser meshes are slightly higher than the results from Anjos et al. [84]. The deceleration stage of the bubble can be observed for all cases with different resolutions, which also exists in the results of Anjos et al. [84]. Except for in the case with the coarse mesh $N = 64$, the rising velocities in cases with higher resolutions reach a stable state and converge to the experimental value from Bhaga and Weber [85].

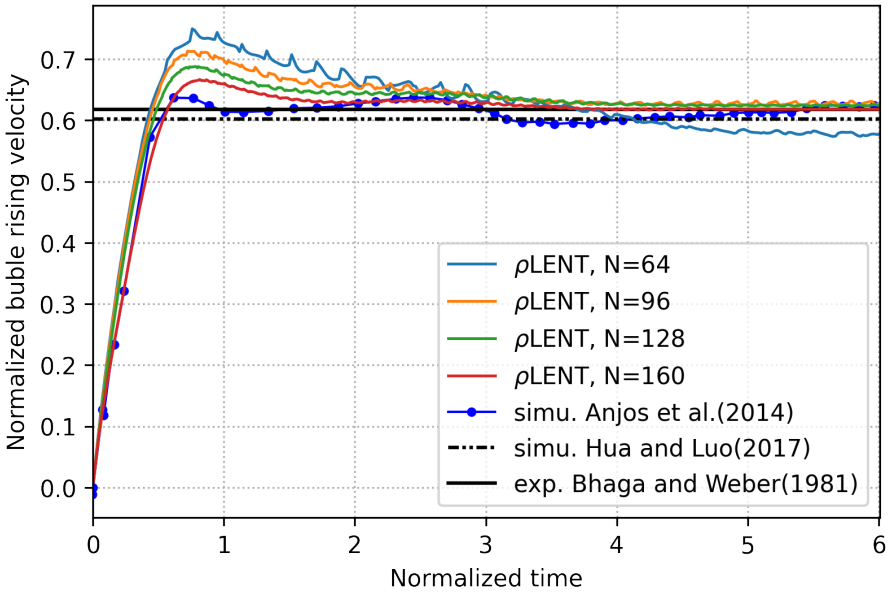

Figure 17: The average bubble velocities from ρLENT with four resolutions are compared with: the experimental results (black solid line) from Bhaga and Weber [85], the simulation results (black dashed double-dotted line) from Hua and Lou [68], and the extracted simulation results (blue solid dotted line) from Anjos et al. [84]. Simu. and exp. are the abbreviation of simulation and experiment.

5. Conclusions

The proposed ρLENT method exactly ensures numerical consistency of the single-field incompressible two-phase momentum convection, discretized by the unstructured collocated Finite Volume Method. The ρLENT method is straightforward and can be applied directly to any two-phase flow simulation method that relies on the collocated FV method for equation discretization of two-phase single-field Navier-Stokes equations by adding a geometrical computation of area fractions α_f^{n+1} from the approximated fluid interface $\tilde{\Sigma}^{n+1}$ and the auxiliary density equation to the solution algorithm. We provide an analysis that connects the mass conservation, phase indicator function conservation and momentum convection, theoretically justifying the numerical consistency of the cell-centered density ρ_c^{n+1} computed by a mass flux identical to the one used in the two-phase momentum convective term. This provides the theoretical reasoning behind the auxiliary mass conservation equation, originally introduced by Ghods and Herrmann [3]. Following the importance of the face-centered (mass flux) density pointed out by Zuzio et al. [7], we derive the expression for the mass flux density using the principle of mass conservation and connect the mass flux density with the phase indicator. We achieve this by avoiding the temporal integration of the conserved property as done very recently by Arrufat et al. [34], which allows us to express the mass fluxes using the phase indicator in a discrete setting. The consistent cell-centered density ρ_c^{n+1} is used in the $p-\mathbf{v}$ coupling algorithm [2] to obtain the velocity $\mathbf{v}_c^{n+1}$, necessary to evolve the fluid interface in the next step from t^{n+1} to t^{n+2}. Once the velocity is obtained by $p-\mathbf{v}$ coupling, the cell-centered density ρ_c^{n+1} is again made consistent with the fluid interface. Using the face-centered (mass-flux)

density in the $p - \mathbf{v}$ coupling and advecting the interface first, enables ρLENT to discretize the momentum convection term implicitly, compared to the explicit convective term discretization that is used by Bussmann et al. [16], Ghods and Herrmann [3] in the collocated Finite Volume setting. The consistency of the mass flux in the auxiliary density equation with the mass flux computed using the phase indicator, justifies theoretically the use of the same interpolation schemes for these two fluxes by Ghods and Herrmann [3], Patel and Natarajan [30], Manik et al. [31].

Results demonstrate the recovery of an exact solution, with the error in the L_∞ norm exactly equaling 0, for the canonical droplet translation verification case studies [75]. Droplets with sub-millimeter diameters and with realistic fluid properties are also advected exactly. Validation cases with realistic surface tension forces and viscosity demonstrate numerical stability of ρLENT, resulting in the relative L_∞ norm for the parasitic currents between 10^{-4} and 10^{-2} for density ratios up to 10^4. Our consistent method successfully recovers the accurate frequency of oscillation for the ellipsoidal droplet with a relative error of 10^{-4}. The simulation also accurately captured the strong deformation of the rising bubble, in excellent agreement with experimental results.

6. Acknowledgments

Funded by the German Research Foundation (DFG) – Project-ID 265191195 – SFB 1194. Calculations for this research were conducted on the Lichtenberg high performance computer of the TU Darmstadt.

References

[1] T. Marić, H. Marschall, D. Bothe, lentFoam–A hybrid Level Set/Front Tracking method on unstructured meshes, Computers & Fluids 113 (2015) 20–31. doi:10.1016/j.compfluid.2014.12.019.

[2] T. Tolle, D. Bothe, T. Marić, SAAMPLE: A segregated accuracy-driven algorithm for multiphase pressure-linked equations, Computers & Fluids 200 (2020) 104450. doi:10.1016/j.compfluid.2020.104450.

[3] S. Ghods, M. Herrmann, A consistent rescaled momentum transport method for simulating large density ratio incompressible multiphase flows using level set methods, Physica Scripta 88 (2013). doi:10.1088/0031-8949/2013/T155/014050.

[4] N. Nangia, B. E. Griffith, N. A. Patankar, A. P. S. Bhalla, A robust incompressible Navier-Stokes solver for high density ratio multiphase flows, Journal of Computational Physics 390 (2019) 548–594. doi:10.1016/j.jcp.2019.03.042. arXiv:1809.01008.

[5] M. Raessi, H. Pitsch, Consistent mass and momentum transport for simulating incompressible interfacial flows with large density ratios using the level set method, Computers and Fluids 63 (2012) 70–81. doi:10.1016/j.compfluid.2012.04.002.

[6] A. Orazzo, J. L. Estivalezes, I. Lagrange, D. Zuzio, A vof-based consistent mass-momentum transport for two-phase flow simulations, in: American Society of Mechanical Engineers, Fluids Engineering Division (Publication) FEDSM, volume 1C-2017, American Society of Mechanical Engineers, 2017, pp. 1–11. doi:10.1115/FEDSM2017-69190.

[7] D. Zuzio, A. Orazzo, J. L. Estivalèzes, I. Lagrange, A new efficient momentum preserving Level-Set/VOF method for high density and momentum ratio incompressible two-phase flows, Journal of Computational Physics 410 (2020) 109342. doi:10.1016/j.jcp.2020.109342.

[8] V. L. Chenadec, H. Pitsch, A 3D unsplit Forward/Backward Volume-of-Fluid approach and coupling to the level set method, J. Comput. Phys. 233 (2013) 10–33. doi:10.1016/j.jcp.2012.07.019.

[9] Unstructured finite-volume level set / front tracking - lent code repository, 2022. URL: https://gitlab.com/leia-methods/lent/-/tree/2022-02-rhoLENT-R1.

[10] X. Li, M. C. Soteriou, High fidelity simulation and analysis of liquid jet atomization in a gaseous crossflow at intermediate Weber numbers, Physics of Fluids 28 (2016) 082101. doi:10.1063/1.4959290.

[11] B. Godderidge, S. Turnock, M. Tan, C. Earl, An investigation of multiphase cfd modelling of a lateral sloshing tank, Computers & Fluids 38 (2009) 183–193. doi:10.1016/j.compfluid.2007.11.007.

[12] S. Soukane, F. Trochu, Application of the level set method to the simulation of resin transfer molding, Composites Science and Technology 66 (2006) 1067–1080. doi:10.1016/j.compscitech.2005.03.001.

[13] Z. Gao, Q. Gao, D. Vassalos, Numerical simulation of flooding of a damaged ship, Ocean Engineering 38 (2011) 1649–1662. doi:10.1016/j.oceaneng.2011.07.020.

[14] O. Desjardins, V. Moureau, Methods for multiphase flows with high density ratio, Center for Turbulence Research Proceedings of the Summer Program (2010) 313–322. URL: https://web.stanford.edu/group/ctr/Summer/SP10/6_02_desjardins.pdf.

[15] M. Rudman, A volume-tracking method for incompressible multifluid flows with large density variations, International Journal for Numerical Methods in Fluids 28 (1998) 357–378. doi:10.1002/(SICI)1097-0363(19980815)28:2<357::AID-FLD750>3.0.CO;2-D.

[16] M. Bussmann, D. B. Kothe, J. M. Sicilian, Modeling high density ratio incompressible interfacial flows, American Society of Mechanical Engineers, Fluids Engineering Division (Publication) FED 257 (2002) 707–713. doi:10.1115/FEDSM2002-31125.

[17] W. J. Rider, D. B. Kothe, Reconstructing volume tracking, Journal of computational physics 141 (1998) 112–152. doi:10.1006/jcph.1998.5906.

[18] G. Cerne, S. Petelin, I. Tiselj, Numerical errors of the volume-of-fluid interface tracking algorithm, International journal for numerical methods in fluids 38 (2002) 329–350. doi:10.1002/fld.228.

[19] M. Sussman, K. M. Smith, M. Y. Hussaini, M. Ohta, R. Zhi-Wei, A sharp interface method for incompressible two-phase flows, Journal of computational physics 221 (2007) 469–505. doi:10.1016/j.jcp.2006.06.020.

[20] M. Sussman, E. G. Puckett, A Coupled Level Set and Volume-of-Fluid Method for Computing 3D and Axisymmetric Incompressible Two-Phase Flows, Journal of Computational Physics 162 (2000) 301–337. doi:10.1006/jcph.2000.6537.

[21] V. Le Chenadec, H. Pitsch, A monotonicity preserving conservative sharp interface flow solver for high density ratio two-phase flows, Journal of Computational Physics 249 (2013) 185–203. doi:10.1016/j.jcp.2013.04.027.

[22] A. Prosperetti, Motion of two superposed viscous fluids, The Physics of Fluids 24 (1981) 1217–1223. doi:10.1063/1.863522.

[23] G. Vaudor, A. Berlemont, T. Ménard, M. Doring, A consistent mass and momentum flux computation method using rudman-type technique with a clsvof solver, in: Fluids Engineering Division Summer Meeting, volume 46230, American Society of Mechanical Engineers, 2014, p. V01CT23A012. doi:10.1115/FEDSM2014-21802.

[24] T. Ménard, S. Tanguy, A. Berlemont, Coupling level set/vof/ghost fluid methods: Validation and application to 3d simulation of the primary break-up of a liquid jet, International Journal of Multiphase Flow 33 (2007) 510–524.

[25] W. Aniszewski, T. Ménard, M. Marek, Volume of fluid (vof) type advection methods in two-phase flow: A comparative study, Computers & Fluids 97 (2014) 52–73. doi:10.1016/j.compfluid.2014.03.027.

[26] G. Vaudor, T. Ménard, W. Aniszewski, M. Doring, A. Berlemont, A consistent mass and momentum flux computation method for two phase flows. Application to atomization process, Computers and Fluids 152 (2017) 204–216. doi:10.1016/j.compfluid.2017.04.023.

[27] M. Owkes, O. Desjardins, A mass and momentum conserving unsplit semi-Lagrangian framework for simulating multiphase flows, Journal of Computational Physics 332 (2017) 21–46. doi:10.1016/j.jcp.2016.11.046.

[28] M. Owkes, O. Desjardins, A computational framework for conservative, three-dimensional, unsplit, geometric transport with application to the volume-of-fluid (VOF) method, J. Comput. Phys. 270 (2014) 587–612. doi:10.1016/j.jcp.2014.04.022.

[29] Z. Yang, M. Lu, S. Wang, A robust solver for incompressible high-reynolds-number two-fluid flows with high density contrast, Journal of Computational Physics (2021) 110474. doi:10.1016/j.jcp.2021.110474.

[30] J. K. Patel, G. Natarajan, A novel consistent and well-balanced algorithm for simulations of multiphase flows on unstructured grids, Journal of Computational Physics 350 (2017) 207–236. doi:10.1016/j.jcp.2017.08.047.

[31] J. Manik, A. Dalal, G. Natarajan, A generic algorithm for three-dimensional multiphase flows on unstructured meshes, International Journal of Multiphase Flow 106 (2018) 228–242. doi:10.1016/j.ijmultiphaseflow.2018.04.010.

[32] M. Alves, P. Oliveira, F. Pinho, A convergent and universally bounded interpolation scheme for the treatment of advection, International journal for numerical methods in fluids 41 (2003) 47–75. doi:10.1002/fld.428.

[33] A. J. Chorin, The numerical solution of the navier-stokes equations for an incompressible fluid, Bulletin of the American Mathematical Society 73 (1967) 928–931.

[34] T. Arrufat, M. Crialesi-Esposito, D. Fuster, Y. Ling, L. Malan, S. Pal, R. Scardovelli, G. Tryggvason, S. Zaleski, A mass-momentum consistent, Volume-of-Fluid method for incompressible flow on staggered grids, Comput. Fluids 215 (2021) 104785. doi:10.1016/j.compfluid.2020.104785.

[35] H. Ding, P. D. Spelt, C. Shu, Diffuse interface model for incompressible two-phase flows with large density ratios, Journal of Computational Physics 226 (2007) 2078–2095. doi:10.1016/j.jcp.2007.06.028.

[36] Y. Wang, C. Shu, J. Y. Shao, J. Wu, X. D. Niu, A mass-conserved diffuse interface method and its application for incompressible multiphase flows with large density ratio, Journal of Computational Physics 290 (2015) 336–351. doi:10.1016/j.jcp.2015.03.005.

[37] Z. Huang, G. Lin, A. M. Ardekani, Consistent, essentially conservative and balanced-force Phase-Field method to model incompressible two-phase flows, Journal of Computational Physics 406 (2020) 109192. doi:10.1016/j.jcp.2019.109192.

[38] T. Inamuro, T. Ogata, S. Tajima, N. Konishi, A lattice boltzmann method for incompressible two-phase flows with large density differences, Journal of Computational physics 198 (2004) 628–644. doi:10.1016/j.jcp.2004.01.019.

[39] T. Lee, C.-L. Lin, A stable discretization of the lattice boltzmann equation for simulation of incompressible two-phase flows at high density ratio, Journal of Computational Physics 206 (2005) 16–47. doi:10.1016/j.jcp.2004.12.001.

[40] H. Zheng, C. Shu, Y.-T. Chew, A lattice boltzmann model for multiphase flows with large density ratio, Journal of computational physics 218 (2006) 353–371. doi:10.1016/j.jcp.2006.02.015.

[41] S. Shin, I. Yoon, D. Juric, The local front reconstruction method for direct simulation of two-and three-dimensional multiphase flows, Journal of Computational Physics 230 (2011) 6605–6646. doi:10.1016/j.jcp.2011.04.040.

[42] T. Marić, D. B. Kothe, D. Bothe, Unstructured un-split geometrical volume-of-fluid methods–a review, Journal of Computational Physics 420 (2020) 109695. doi:10.1016/j.jcp.2020.109695.

[43] J. U. Brackbill, D. B. Kothe, C. Zemach, A continuum method for modeling surface tension, Journal of computational physics 100 (1992) 335–354. doi:10.1016/0021-9991(92)90240-Y.

[44] T. Tolle, D. Gründing, D. Bothe, T. Marić, triSurfaceImmersion: Computing volume fractions and signed distances from triangulated surfaces immersed in unstructured meshes, Computer Physics Communications 273 (2022) 108249.

[45] H. Jasak, Error analysis and estimation for the finite volume method with applications to fluid flows. (1996). URL: http://hdl.handle.net/10044/1/8335.

[46] C. Hirsch, Numerical computation of internal and external flows, Wiley, 1997. doi:10.1016/B978-0-7506-6594-0.X5037-1.

[47] F. Moukalled, L. Mangani, M. Darwish, et al., The finite volume method in computational fluid dynamics, volume 113, Springer, 2016. doi:10.1007/978-3-319-16874-6.

[48] H. Jasak, A. Jemcov, Z. Tukovic, et al., Openfoam: A c++ library for complex physics simulations, in: International workshop on coupled methods in numerical dynamics, volume 1000, IUC Dubrovnik Croatia, 2007, pp. 1–20.

[49] H. Jasak, Openfoam: open source cfd in research and industry, International Journal of Naval Architecture and Ocean Engineering 1 (2009) 89–94. doi:10.2478/IJNAOE-2013-0011.

[50] T. Marić, J. Höpken, K. G. Mooney, The OpenFOAM Technology Primer, Zenodo, 2021. doi:10.5281/zenodo.4630596.

[51] S. Shin, D. Juric, Modeling three-dimensional multiphase flow using a level contour reconstruction method for front tracking without connectivity, Journal of Computational Physics 180 (2002) 427–470. doi:10.1006/jcph.2002.7086.

[52] S. Shin, S. Abdel-Khalik, V. Daru, D. Juric, Accurate representation of surface tension using the level contour reconstruction method, Journal of Computational Physics 203 (2005) 493–516. doi:10.1016/j.jcp.2004.09.003.

[53] H. D. Ceniceros, A. M. Roma, A. Silveira-Neto, M. M. Villar, et al., A robust, fully adaptive hybrid level-set/front-tracking method for two-phase flows with an accurate surface tension computation, Commun Comput Phys 8 (2010) 51–94. doi:10.4208/cicp.050509.141009a.

[54] S. Shin, J. Chergui, D. Juric, A solver for massively parallel direct numerical simulation of three-dimensional multiphase flows, Journal of Mechanical Science and Technology 31 (2017) 1739–1751. doi:10.1007/s12206-017-0322-y.

[55] T. Marić, J. Höpken, K. G. Mooney, The OpenFOAM Technology Primer, Zenodo, 2021. doi:10.5281/zenodo.4630596.

[56] F. Moukalled, L. Mangani, M. Darwish, et al., The finite volume method in computational fluid dynamics:An Advanced Introduction with OpenFOAM® and Matlab®, volume 6, Springer, 2016, pp. 443–450. doi:10.1007/978-3-319-16874-6.

[57] C. B. Ivey, P. Moin, Conservative and bounded volume-of-fluid advection on unstructured grids, J. Comput. Phys. 350 (2017) 387–419. URL: http://dx.doi.org/10.1016/j.jcp.2017.08.054. doi:10.1016/j.jcp.2017.08.054.

[58] T. Marić, H. Marschall, D. Bothe, An enhanced un-split face-vertex flux-based VoF method, J. Comput. Phys. 371 (2018) 967–993. doi:10.1016/j.jcp.2018.03.048.

[59] H. Scheufler, J. Roenby, Accurate and efficient surface reconstruction from volume fraction data on general meshes, Journal of computational physics 383 (2019) 1–23. URL: https://doi.org/10.1016/j.jcp.2019.01.009. doi:10.1016/j.jcp.2019.01.009.

[60] T. Marić, D. B. Kothe, D. Bothe, Unstructured un-split geometrical volume-of-fluid methods–a review, Journal of Computational Physics 420 (2020) 109695. doi:10.1016/j.jcp.2020.109695.

[61] M. Muradoglu, G. Tryggvason, A front-tracking method for computation of interfacial flows with soluble surfactants, Journal of computational physics 227 (2008) 2238–2262. doi:10.1016/j.jcp.2007.10.003.

[62] G. Tryggvason, B. Bunner, A. Esmaeeli, D. Juric, N. Al-Rawahi, W. Tauber, J. Han, S. Nas, Y.-J. Jan, A front-tracking method for the computations of multiphase flow, Journal of computational physics 169 (2001) 708–759. doi:https://doi.org/10.1006/jcph.2001.6726.

[63] G. M. Treece, R. W. Prager, A. H. Gee, Regularised marching tetrahedra: improved iso-surface extraction, Computers & Graphics 23 (1999) 583–598.

[64] M. Detrixhe, T. D. Aslam, From level set to volume of fluid and back again at second-order accuracy, International Journal for Numerical Methods in Fluids 80 (2016) 231–255. doi:10.1002/fld.4076.

[65] R. I. Issa, Solution of the implicitly discretised fluid flow equations by operator-splitting, Journal of computational physics 62 (1986) 40–65. URL: https://doi.org/10.1016/0021-9991(86)90099-9. doi:10.1016/0021-9991(86)90099-9.

[66] S. V. Patankar, D. B. Spalding, A calculation procedure for heat, mass and momentum transfer in three-dimensional parabolic flows, International Journal of Heat and Mass Transfer 15 (1972) 1787–1806. doi:10.1016/0017-9310(72)90054-3.

[67] R. Singh, W. Shyy, Three-dimensional adaptive Cartesian grid method with conservative interface restructuring and reconstruction, Journal of Computational Physics 224 (2007) 150–167. URL: https://linkinghub.elsevier.com/retrieve/pii/S002199910600622X. doi:10.1016/j.jcp.2006.12.026.

[68] J. Hua, J. Lou, Numerical simulation of bubble rising in viscous liquid, Journal of Computational Physics 222 (2007) 769–795. URL: https://linkinghub.elsevier.com/retrieve/pii/S0021999106003949. doi:10.1016/j.jcp.2006.08.008.

[69] J. Hua, J. F. Stene, P. Lin, Numerical simulation of 3D bubbles rising in viscous liquids using a front tracking method, Journal of Computational Physics 227 (2008) 3358–3382. URL: https://linkinghub.elsevier.com/retrieve/pii/S0021999107005530. doi:10.1016/j.jcp.2007.12.002.

[70] M. Pivello, M. Villar, R. Serfaty, A. Roma, A. Silveira-Neto, A fully adaptive front tracking method for the simulation of two phase flows, International Journal of Multiphase Flow 58 (2014) 72–82. URL: https://linkinghub.elsevier.com/retrieve/pii/S0301932213001286. doi:10.1016/j.ijmultiphaseflow.2013.08.009.

[71] J. Liu, T. Tolle, T. Maric, A consistent discretization of the single-field two-phase momentum convection term for the unstructured finite volume Level Set / Front Tracking method - data, 2022. URL: https://doi.org/10.5281/zenodo.6092417. doi:10.5281/zenodo.6092417.

[72] J. Liu, T. Tolle, T. Maric, A consistent discretization of the single-field two-phase momentum convection term for the unstructured finite volume Level Set / Front Tracking method - source code, 2022. URL: https://doi.org/10.5281/zenodo.6091930. doi:10.5281/zenodo.6091930.

[73] J. Liu, T. Tolle, T. Maric, LEvel Set / froNT tracking - LENT GitLab repository, https://gitlab.com/leia-methods/lent/-/tree/2022-02-rhoLENT-R1, 2022.

[74] F. Denner, B. G. van Wachem, Numerical time-step restrictions as a result of capillary waves, Journal of Computational Physics 285 (2015) 24–40. doi:10.1016/j.jcp.2015.01.021.

[75] S. Popinet, An accurate adaptive solver for surface-tension-driven interfacial flows, Journal of Computational Physics 228 (2009) 5838–5866. doi:10.1016/j.jcp.2009.04.042.

[76] A. W. Adamson, A. P. Gast, et al., Physical chemistry of surfaces, 6th Edition, volume 150, New York: Wiley, 1997.

[77] R. Zivojnovic, Silicone oil in vitreoretinal surgery, volume 12, Springer Science & Business Media, 2012.

[78] E. Trinh, T. Wang, Large-amplitude free and driven drop-shape oscillations: experimental observations, Journal of Fluid Mechanics 122 (1982) 315–338. doi:10.1017/S0022112082002237.

[79] H. Lamb, Hydrodynamics (New York, Dover Publications, 1932).

[80] S. Chandrasekhar, The oscillations of a viscous liquid globe, Proceedings of the London Mathematical Society 3 (1959) 141–149.

[81] C. Miller, L. Scriven, The oscillations of a fluid droplet immersed in another fluid, Journal of fluid mechanics 32 (1968) 417–435.

[82] A. Prosperetti, Normal-mode analysis for the oscillations of a viscous liquid drop in an immiscible liquid (1980).

[83] W. Hiller, T. Kowalewski, Experimental analysis of free oscillating liquid drops, in: Proceedings of the 10th Australasian Fluid Mechanics Conference, University of Melbourne, 1989, pp. 7–21.

[84] G. Anjos, N. Borhani, N. Mangiavacchi, J. Thome, A 3d moving mesh finite element method for two-phase flows, Journal of Computational Physics 270 (2014) 366–377. URL: https://www.sciencedirect.com/science/article/pii/S0021999114002551. doi:https://doi.org/10.1016/j.jcp.2014.03.067.

[85] D. Bhaga, M. E. Weber, Bubbles in viscous liquids: shapes, wakes and velocities, Journal of Fluid Mechanics 105 (1981) 61–85. doi:10.1017/S002211208100311X.

Appendix A. Full figures of the results from translating droplet cases

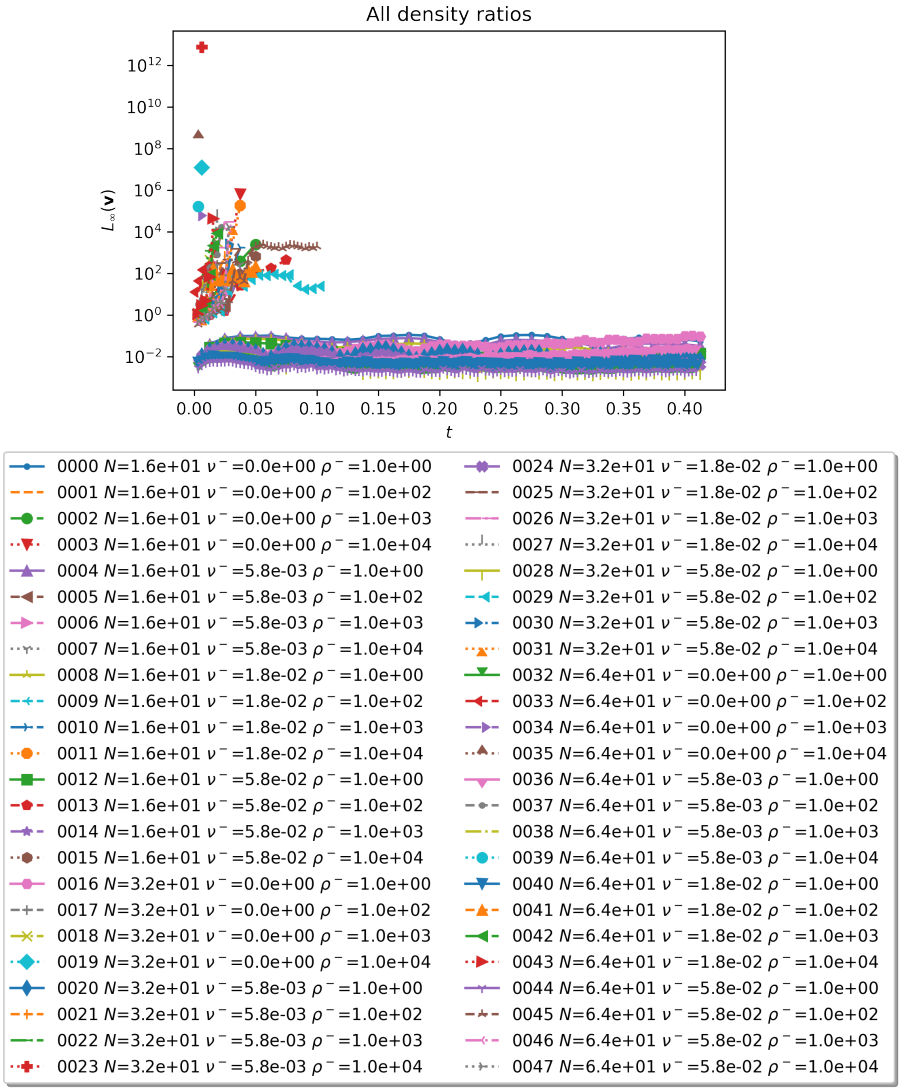

Figure A.18: Full figure of fig. 11a

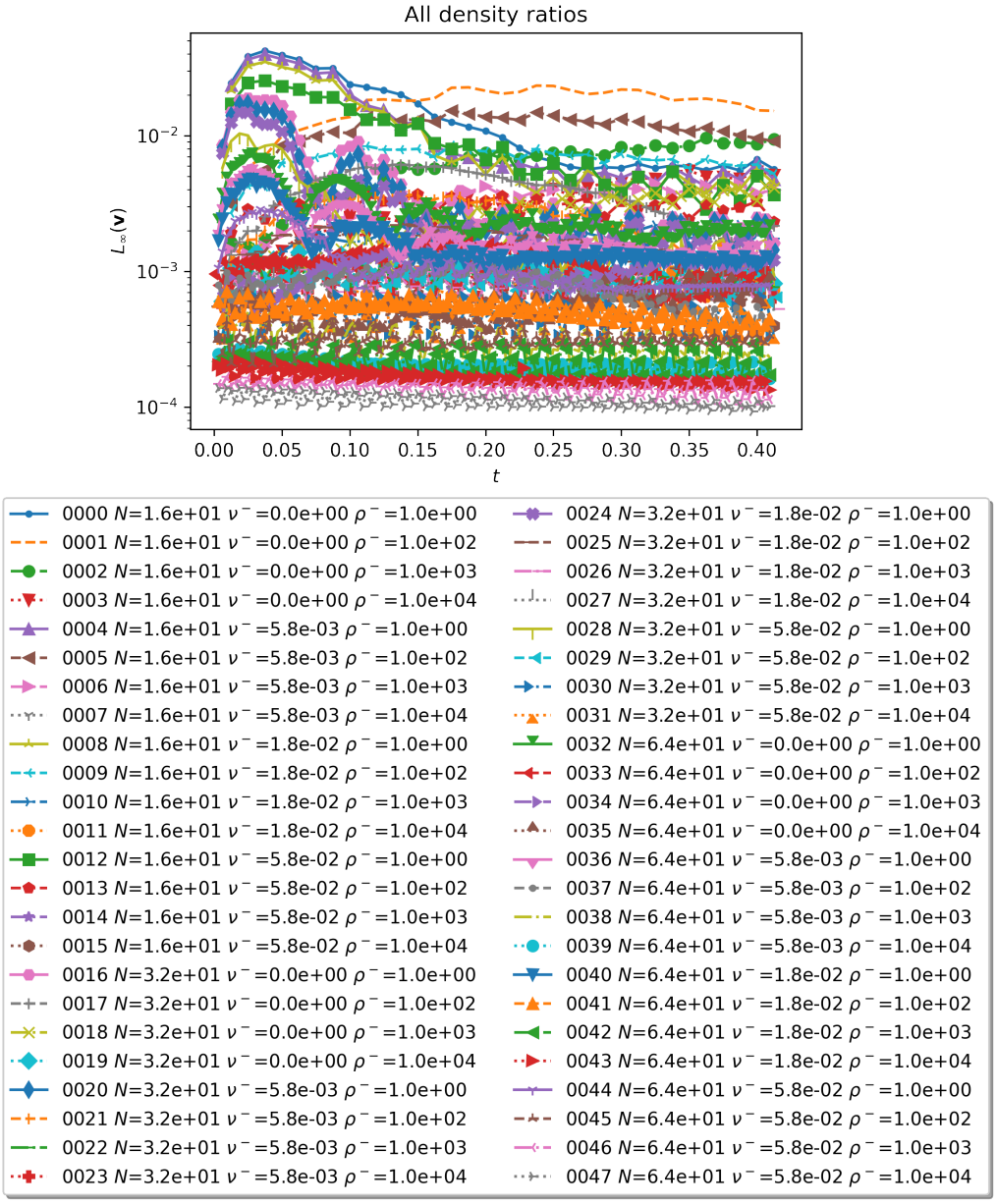

Figure A.19: Full figure of fig. 11b

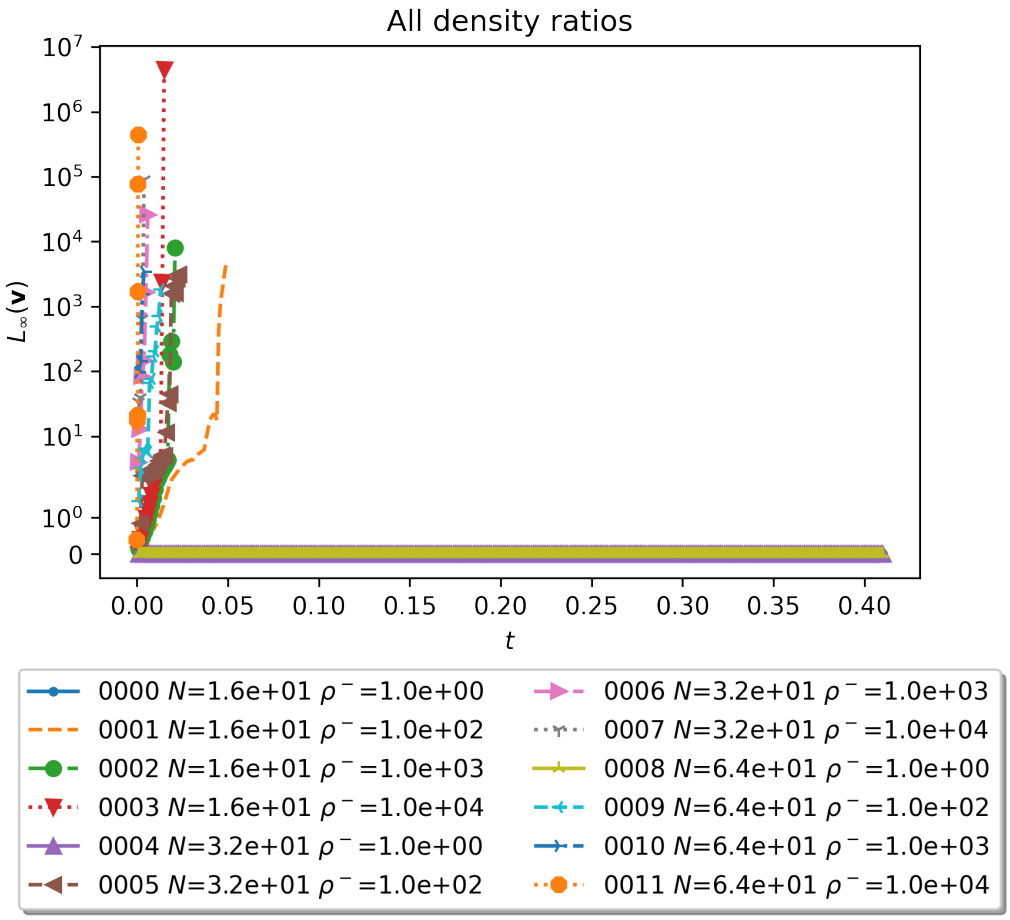

Figure A.20: Full figure of fig. 9a